Contributions to Mineralogy and Petrology (2024) 179:71
https://doi.org/10.1007/s00410-024-02132-1

ORIGINAL PAPER

Experimental constraints on the nature of multiphase solid inclusions and their bearing on mantle wedge metasomatism, Bohemian Massif

Antonio Acosta-Vigil[1,2,3,8] · Jana Kotková[4,5] · Renata Čopjaková[5] · Richard Wirth[6] · Jörg Hermann[3,7]

Received: 7 November 2023 / Accepted: 15 April 2024 / Published online: 21 June 2024

Abstract

This study tests experimentally the hypothesis that calculated bulk compositions of multiphase solid inclusions present in minerals of ultrahigh pressure rocks, can be equated to the composition of the former trapped fluids. We investigated samples from the ultrahigh pressure garnet peridotites of the Bohemian Massif, spatially associated with ultrahigh pressure crustal rocks and representing a former subduction interface environment. Inclusions present in garnets, composed of amphibole + Ba-mica kinoshitalite + carbonates (dolomite + magnesite + norsethite), were taken to their entrapment conditions of c. 4.5 GPa and 1075 ºC. They (re)crystallized into a garnet fringe at the boundary between inclusion and host garnet, kinoshitalite ± olivine, carbonatite melt, and a hydrous fluid. Although the latter may have exsolved from the carbonatite melt upon quenching, microstructures suggest it was present at trapped conditions, and mass balance indicates that it corresponds to a Na-K-Cl-F-rich saline aqueous fluid (brine). Experiments demonstrate the stability of kinoshitalite at 4.5 GPa and 1075 ºC, and suggest that Ba-rich mica + carbonatite melt + brine coexisted at near-peak conditions. Barium is compatible in the carbonatite melt and mica with respect to the brine, with a partition coefficient between carbonatite melt and mica of ≈ 2.5–3. The garnet fringe formed from incongruent reaction of the former inclusion assemblage due to reversing the fluid(s)-host garnet reaction that occurred upon natural cooling/decompression. Loss of H_2 or H_2O from the inclusions due to volume diffusion through garnet and/or decrepitation, during geological timeframes upon decompression/cooling, may have prevented rehomogenization to a single homogeneous fluid. Our study shows that great care is needed in the interpretation of multiphase solid inclusions present in ultrahigh pressure rocks.

Keywords Subduction · Mantle metasomatism · Multiphase solid inclusions · Remelting experiments · Carbonatite melt · Barium partitioning

Communicated by Othmar Müntener.

✉ Antonio Acosta-Vigil
a.acosta@csic.es

[1] Instituto Andaluz de Ciencias de la Tierra (IACT), CSIC, Granada, Spain

[2] Dipartimento di Geoscienze, Universitá di Padova, Padua, Italy

[3] Research School of Earth Sciences, The Australian National University, Acton, Australia

[4] Czech Geological Survey, Prague, Czech Republic

[5] Department of Geological Sciences, Masaryk University, Brno, Czech Republic

[6] 3.5 Interface Geochemistry, GFZ German Research Centre for Geosciences, Potsdam, Germany

[7] Institute of Geological Sciences, University of Bern, Bern, Switzerland

[8] Malta Consolider Team, Madrid, Spain

Introduction

Subduction zones are key geodynamic settings regarding the mass transfer between the deep mantle and Earth's crust/lithosphere. Characterizing elemental exchange during subduction processes is fundamental to understand the petrological and geochemical differentiation of Earth. Fluids are the primary agents for transferring mass between the subducted crustal slab and the overlying mantle wedge, and within the mantle wedge that eventually melts and contributes to crustal growth by feeding volcanic arcs (e.g. Wyllie 1988; Arculus 1994; Tatsumi and Eggins 1995; Schmidt and Poli 1998). Though highly fugitive, these fluids can be captured as primary inclusions within minerals crystallizing during subduction processes (Philippot 1993, and references therein). Some of these inclusions are characterized by the presence of a high proportion and variety of minerals,

hence by high concentrations of solute in the former trapped fluid (Philippot 1993; Stöckhert et al. 2001). They have been referred to as dense hydrous silicates, polyphase inclusions, or multiphase solid inclusions (MSI; Frezzotti and Ferrando 2015, and references therein).

Recently, Čopjaková and Kotková (2018) and Kotková et al. (2021) have described the presence of MSI in garnets of subduction-related samples, represented by ultra-high pressure (UHP) peridotites of the Bohemian Massif. These peridotites equilibrated at peak pressures of c. 4 GPa (Medaris et al. 2015), and are interpreted as part of the mantle lithospheric wedge during the Variscan subduction and collision of northern Gondwana underneath Laurasia (Medaris et al. 2005, 2015). Kotková et al. (2021) have approached the composition of the trapped fluids from mass balance, using detailed (FEG-SEM BSE) two-dimensional (2D) modal analysis of the MSI combined with EPMA analysis of their minerals. They conclude that the MSI represent carbonate–silicate liquids produced after: (i) partial UHP crystallization of an intruding parental carbonate–silicate melt that formed garnet pyroxenite veins in the host peridotites; and (ii) later migration through, and interaction of the residual liquid with the host peridotites, producing their metasomatism.

Multiphase solid inclusions can preserve and record the precise nature of trapped fluids provided that, after entrapment, inclusions behave as closed systems, i.e. there is neither any significant mass loss from inclusions due to decrepitation and/or diffusion through the host mineral, nor reaction between fluids/crystallized products and the host (Roedder 1984; Touret 2001; Stöckhert et al. 2001; Hermann et al. 2013; Frezzotti and Ferrando 2015). Experimental remelting of MSI is one of the best procedures to investigate the precise nature of trapped fluids, and to test if modal and mineral analyses of MSI can retrieve the composition of these fluids.

This study expands and complements that of Kotková et al. (2021) testing experimentally their interpretation, by remelting MSI present in garnets of an UHP Bohemian Massif peridotite. The results show that MSI do not rehomogenize to a single fluid phase but systematically transform to a garnet fringe higher in Mg# and a Ba-rich mica ± olivine, both coexisting with a carbonatite melt and an aqueous fluid. The experiments indicate that bulk compositions of primary multiphase solid inclusions in UHP rocks should not be directly equated to the composition of the originally trapped matrix fluid.

Geological background

The studied garnet peridotite pertains to the Saxothuringian zone of the Bohemian Massif. Previous studies at the scale of this massif have shown that such peridotites constitute lenses that contain layers of garnet pyroxenite and eclogite. They are spatially associated with high-temperature (HT) eclogites and high-pressure (HP)-to-UHP felsic granulites, and likely represent fragments of a subcontinental lithospheric mantle wedge above a subduction zone (Schmädicke et al. 1992; Schmädicke and Evans 1997; Massonne 2001; Medaris et al. 2005). High P-to-UHP metamorphism of the granulites documents subduction of continental crust down to the base of the continental lithosphere (c. 150 km; Massonne and O'Brien 2003; Kotková et al. 2011; Haifler and Kotková 2016). This setting provides an excellent natural laboratory to study the interaction between subducting crust and overlying mantle wedge.

The studied peridotite sample was drilled in the Saxothuringian basement c. 25 km to the SE of the Erzgebirge Crystalline Complex (T-7 borehole, 500 m deep, Fig. 1; see Medaris et al. 2015). The drill encountered a 114 m thick (perpendicular to layering), dipping peridotite body made of alternating meter- to decameter-thick layers of harzburgites and lherzolites, except for a ≤ 1 cm-thick vein of pyroxenite within harzburgite towards the top, and two layers of eclogite and a vein of pyroxenite within lherzolite towards the bottom. The ultramafic rocks appear sandwiched within, and are concordant with respect to felsic diamond-bearing UHP granulites. Peridotites and host granulites record peak conditions of c. 1030–1150 ºC/3.6–5.5 GPa, and c. 1100 ºC/4.5–5.0 GPa, respectively (Kopecký and Sattran 1966; Fiala and Paděra 1977; Kotková et al. 2011; Medaris et al. 2015; Haifler and Kotková 2016; Haifler et al. 2024).

Host rocks

Medaris et al. (2015) studied the petrology and geochemistry of fifteen samples between borehole depths of 221–434 m, labelling samples using rock type and depth. Both lherzolites and harzburgites show inequigranular textures with frequent large (≤ 5 mm) rounded garnets and rare orthopyroxene and clinopyroxene porphyroclasts (> 1 mm), irregularly distributed within a fine-grained (≤ 1 mm) granoblastic matrix of olivine, orthopyroxene and clinopyroxene (Fig. 2a–b). Peridotites are extensively serpentinized (Medaris et al. 2015; Haifler et al. 2024). The pyroxenite vein located towards the top (pyroxenite 256, hereafter Px 256, Fig. 1) is composed of coarse-grained garnet (60 vol. %), clinopyroxene (35%), together with several vol. % of phlogopite and subordinate pargasitic amphibole, both minerals concentrated at the contact with host harzburgite 256 (hereafter Hz 256). Phlogopite and amphibole are also present at the rims of garnets and interstitial in the pyroxenite matrix. The Hz 256 is enriched in orthopyroxene and garnet with respect to other harzburgites further away from Px 256. Phlogopite ± pargasitic amphibole are also present as either thin discontinuous veins or dispersed crystals in the matrix of lherzolites adjacent to the eclogites, and in the pyroxenite vein found

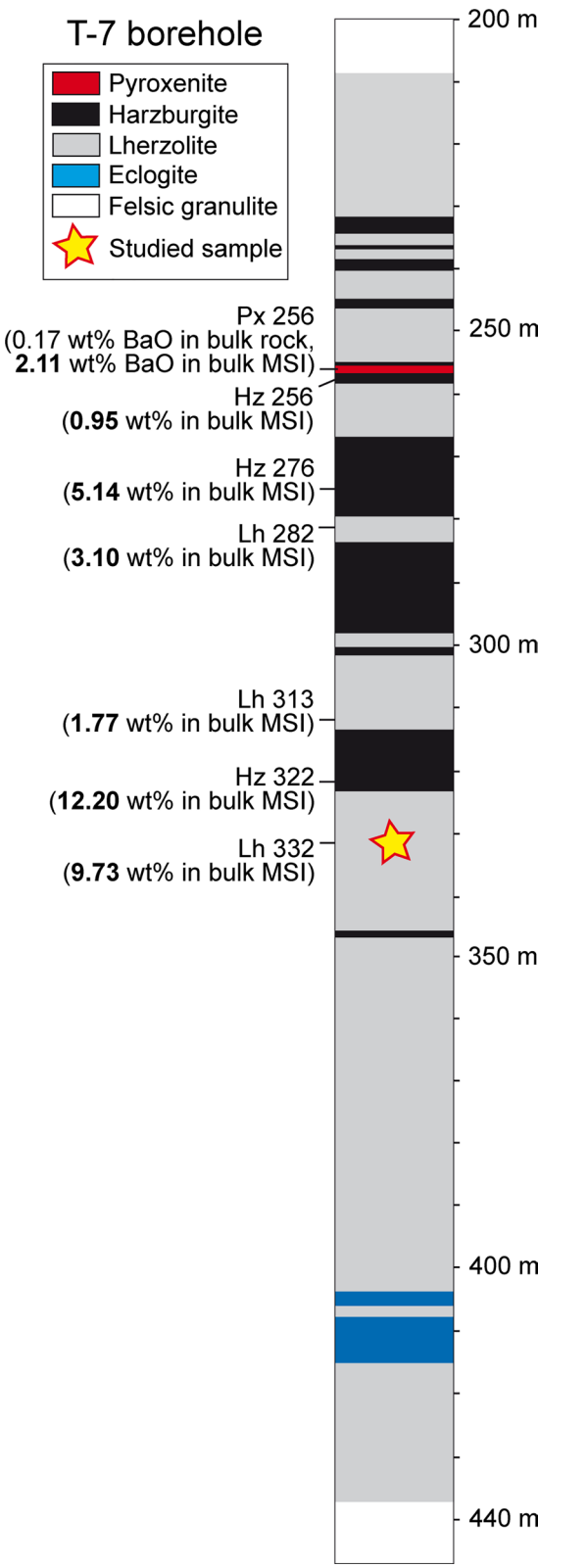

Fig. 1 Profile of the T-7 borehole, showing the distribution of rock types with respect to depth, and the location of samples with multiphase solid inclusions (MSI) studied by Kotková et al. (2021). Numbers next to samples refer to wt% BaO either measured in the bulk rock or calculated for the bulk of the MSI present in the sample (Kotková et al. 2021). Yellow star shows the location of the experimentally studied sample. Modified from Medaris et al. (2015) and Kotková et al. (2021)

at the bottom of the ultramafic body (Fig. 1) (Medaris et al. 2015; Kotková et al. 2021).

Compared to the primitive mantle, all peridotites are variably enriched in Cs, Th, U and Pb (± LREE). Some lherzolites show similar major and trace element concentrations to primitive mantle, whereas other lherzolites and the harzburgites are depleted in Al, Ca, Ti, Si, Sr, Nb, Ta, Zr, Hf, MREE, HREE. The Px 256 shows about 20-fold enrichment in K and Rb, extreme enrichment (> 50-100x) in Th, U, Pb, Ba, H_2O, CO_2 and LREE, and a pronounced negative Nb–Ta anomaly (Medaris et al. 2015; Kotková et al. 2021). Based on the geologic context, rock association and peridotite compositions, the ultramafic body is interpreted as relict primitive mantle lherzolites affected by moderate to strong degrees of Proterozoic partial melting, that were subsequently refertilized (mostly cryptically) by subduction-related melts in the stability field of garnet. Percolating melts would be represented by the thin layer of Px 256. The small-scale layering between lherzolites and harzburgites is interpreted as due to deformation, likely during the Variscan subduction; percolation of metasomatizing melts likely occurred contemporaneously to deformation (Medaris et al. 2015).

Multiphase solid inclusions

Čopjaková and Kotková (2018) and Kotková et al. (2021) have studied the microstructures, mineralogy, and mineral compositions of c. 90 MSI present in garnets of the pyroxenite vein Px 256, its host harzburgite Hz 256, and five samples of lherzolites and harzburgites located at increasing distance from Px 256 (Fig. 1). The MSI appear either randomly distributed throughout the entire garnet (Px 256), or within an annulus at the rim of garnet (all studied peridotites). They range in size between ≈ 5–40 µm, with isometric to elongated, often negative crystal shapes. The MSI are mostly composed of hornblende (except in Hz 322, with clinopyroxene instead), the Ba-mica kinoshitalite, dolomite and magnesite, with variable but generally low proportions of apatite, spinel, norsethite, Ba-feldspar, clinopyroxene, orthopyroxene and garnet II. Garnet II is slightly higher in Al and Mg#, and slightly lower in Ca, Ti, Cr with respect to host garnet. They

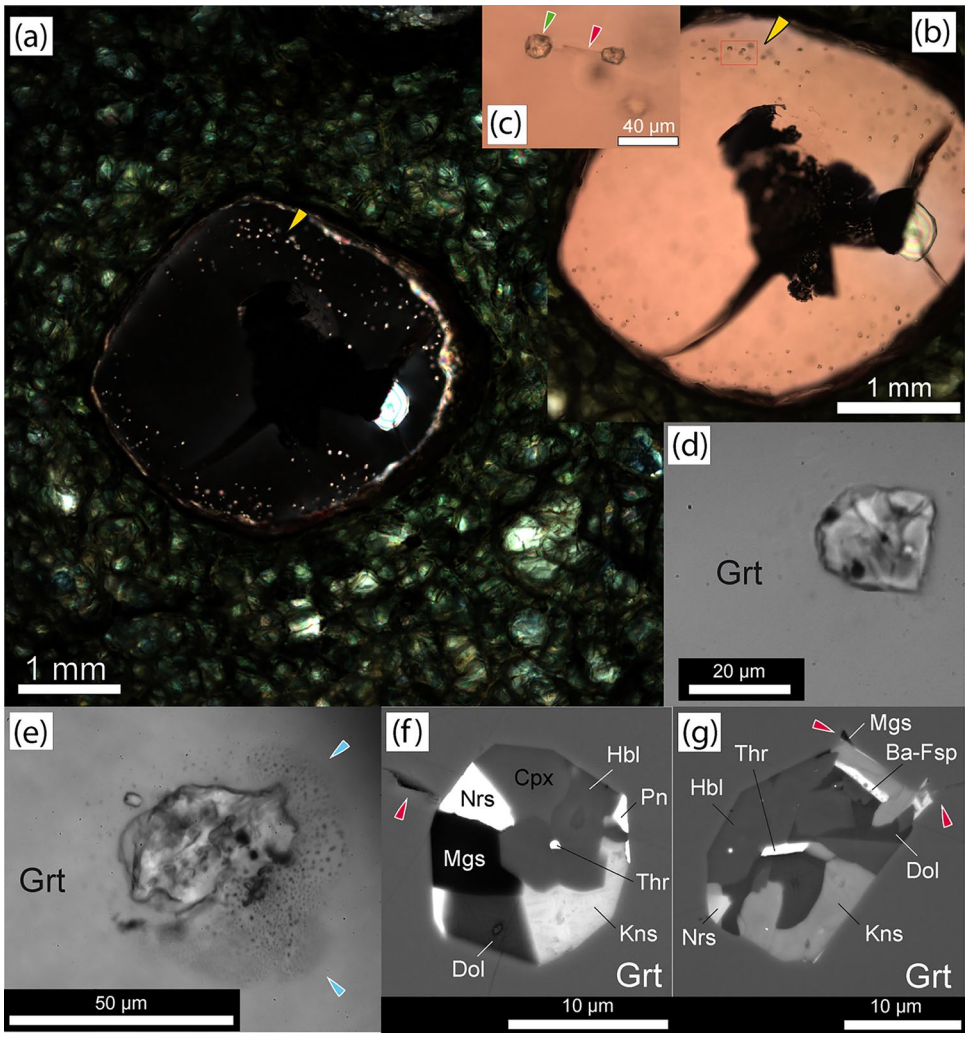

Fig. 2 Optical microscope photomicrograph (**a**–**e**; a, in cross-polarized light; **b**–**e**, in plane-polarize light) and scanning electron microscope images (backscattered electrons, **f**–**g**) of the studied lherzolite 332 and garnets with MSI. **a**–**b** Detail of one of the studied garnets, set in a fine-grained matrix and showing the primary character of the MSI (yellow arrow) constituting an annulus at its rim. **c** Detail of garnet in (**b**) (red rectangle) showing MSI with euhedral shapes and apparently with (red arrow) or without (green arrows) decrepitation microstructures. **d**–**g** Details of MSI in garnets: euhedral to subhedral inclusion without decrepitation microstructures (**d**); subhedral to anhedral inclusion with decrepitation products such as haloes of small former fluid inclusions (blue arrows) (**e**); euhedral inclusion without decrepitation microstructures, red arrow points to a nearby empty void (**f**); euhedral to subhedral inclusion with clear decrepitation microstructures such as offshoots (red arrows) (**g**). See also Supplementary Fig. 1

also contain traces of monazite, rutile, ilmenite, graphite, scheelite, thorianite, uraninite, pentlandite and chalcopyrite. Tiny voids may be present in c. 20% of studied MSI, constituting on average ≈ 0.14 vol.%.

The bulk compositions of MSI without significant decrepitation within each studied rock sample are quite variable according to the relative proportions of silicates vs. carbonates, which Kotková et al. (2021) attribute to an artifact associated with 2D studies on heterogeneous three-dimensional inclusions. Using the average bulk composition of MSI found within each sample, they obtain silicate-carbonate compositions that, with increasing distance to the Px 256 vein, roughly evolve towards higher bulk concentrations of K, Ba and CO_2 (Fig. 1).

Studied sample

We have experimentally investigated MSI hosted in garnets from lherzolite 332 (hereafter Lh 332, Fig. 1). The MSI are dominated by hornblende, kinoshitalite and carbonates (dolomite > magnesite and norsethite), with minor clinopyroxene, garnet II and Ba-feldspar, and accessory apatite, thorianite/uraninite, monazite, graphite, pentlandite and scheelite. The MSI in Lh 332 are primary as they occupy a ≈ 100–1000 µm wide annulus at the rim of garnets (Fig. 2a–b; see Roedder 1984). Inclusions range in size between ≈ 5–30 µm and are frequently in apparent microstructural equilibrium with the host garnet as they often show negative crystal shapes (Fig. 2c, d, f; Supplementary Fig. 1a). Clear decrepitation microstructures such as offshoots (Fig. 2c, g; Supplementary Fig. 1b-d) and, less commonly, haloes of small inclusions (Fig. 2e; Supplementary Fig. 1c), are visible under the optical and scanning electron microscope in c. 30–40% of the MSI (compare with Fig. 2d, f, and Supplementary Fig. 1a, without visible decrepitation microstructures). Scanning electron microscope, FIB-TEM and Raman spectroscopy studies on decrepitated MSI in lherzolites show that offshoots and haloes of small inclusions are composed of the main mineral components of the studied inclusions: magnesite,

graphite, kinoshitalite, Ba feldspar and rare NaCl (Fig. 2g; Supplementary Fig. 1c-d). It is important to note that decrepitated MSI show similar mineral assemblages and proportions with respect to apparently undecrepitated MSI (compare Fig. 2f and Supplementary Fig. 1a, with Fig. 2g and Supplementary Fig. 1c-d; and with Fig. 4 of Čopjaková and Kotková 2018, Fig. 4 of Kotková et al. 2021).

Composition of garnet, conditions of MSI entrapment and experimental P–T

Garnets from Lh 332 show flat compositional profiles, except for: (i) an inner rim, ≈ 250–1000 µm wide, showing a slight to moderate increase in Fe and decrease in Mg and Mg# compared to flat core compositions; and (ii) a very narrow outer rim, ≈ 50–200 µm from the edge, with a sharp increase in Fe and decrease in Mg and Mg# (Supplementary Fig. 2). The MSI-bearing garnet annulus generally occupies the inner rim (see also Fig. 3 of Čopjaková and Kotková 2018).

Previously calculated peak metamorphic conditions for all studied peridotite samples from the coherent ultramafic layer range between 3.6 and 4.8 GPa and 1030–1150 ºC (Medaris et al. 2015). Peak P–T conditions for the studied lherzolite 332 sample correspond to 3.6 GPa and 1030 °C, using the iterative solution; or 3.8–4.0 GPa and 940–1050 °C, using a variety of classical geothermobarometers (Medaris et al. 2015). New P–T estimations from Haifler et al. (2024) for the MSI-rich garnet rims in peridotites, using compositions of the rare pyroxene porphyroclast rims and MSI-bearing garnet domains, vary within the range 950–1050 °C and 4–4.5 GPa, similar to the previous peak P–T estimates by Medaris et al. (2015) who used the fine-grained matrix mineral compositions for their calculations.

Microstructures indicate that MSI are primary and were trapped late in the history of garnet crystallization, during growth of rims (see above, Fig. 2, Supplementary Fig. 2; Čopjaková and Kotková 2018; Kotková et al. 2021). Garnet profiles are probably affected to some extent by volume diffusion during the retrograde path, i.e. garnet compositional profiles might not entirely correspond to growth profiles. However, it is reasonable to consider that MSI were trapped within the range of 950–1050 °C and 4–4.5 GPa (Haifler et al. 2024). We conducted experiments at 1000 °C, 1075 °C and 1225 °C, and P of 4–4.5 GPa. These experimental T cover the lower (950 °C) and upper (1050 °C) ends of the T range determined for the MSI-bearing garnet rim, as well as T well above (c. 150–200 °C) this range. Experimental P of 4.5 GPa used in most experiments is similar to the highest value determined for the crystallization of the MSI-bearing garnet annulus, and guarantees that inclusions did not decrepitate during the experiments (see below).

Methods

Experimental rehomogenization of multiphase solid inclusions

Experiments were conducted in a piston cylinder apparatus at the Research School of Earth Sciences (RSES) at The Australian National University (ANU). The methodology follows Cesare et al. (2015) (see also Malaspina et al. 2006; Bartoli et al. 2013), with appropriate improvements to account for the particular nature of the investigated system (see below). Double polished ≈ 300 µm-thick sections were used to obtain single MSI-bearing garnet chips containing entirely enclosed MSI. Chips were selected from four garnet crystals of a single Lh 332 thick section. Experiments were conducted without added H_2O to the capsule. However, we observed after conducting the first experiment D2667 that garnet chips recrystallized at the edges and along veins (former fractures). Frequent trails of secondary fluid inclusions (FI) with similar orientations to the veins appeared also crosscutting the garnet. We concluded that these features were likely due to percolation of, and reaction with H_2O unintentionally introduced to the runs, either adsorbed at the surface of starting materials or decomposed from traces of matrix serpentine attached to garnet rim chips (e.g. London et al. 2012; Mangan et al. 2021; see section Results).

Garnet chips were loaded into 2.8 mm inner diameter gold capsules, embedded in graphite powder to isolate the chips from each other and from the capsule walls. Previous rehomogenization experiments used powders of either host bulk rock (Malaspina et al. 2006) or silica (Cesare et al. 2015), that recrystallized and formed a solid matrix cementing all garnet fragments after quenching, impeding further manipulation of the fragments. This is highly inconvenient when inclusions in garnet are scarce, as in this case. During our experiments graphite powder recrystallized but remained as an unconsolidated material. Hence individual garnet chips were recovered and mounted for analysis maximizing the exposed garnet surface, and therefore the potential number of exposed inclusions upon polishing. After examining run D2667 with metasomatic veins and trails of secondary FI, all materials (capsule, graphite powder, garnet chips) used in the rest of experiments were kept a few hours in a furnace at 120 ºC right before loading and welding the capsules, to minimize water adsorbed at surfaces. We also ensured that no visible traces of matrix serpentine were attached to garnet rim chips. Both strategies described above were important to successfully conduct the experimental study of MSI in this ultramafic system.

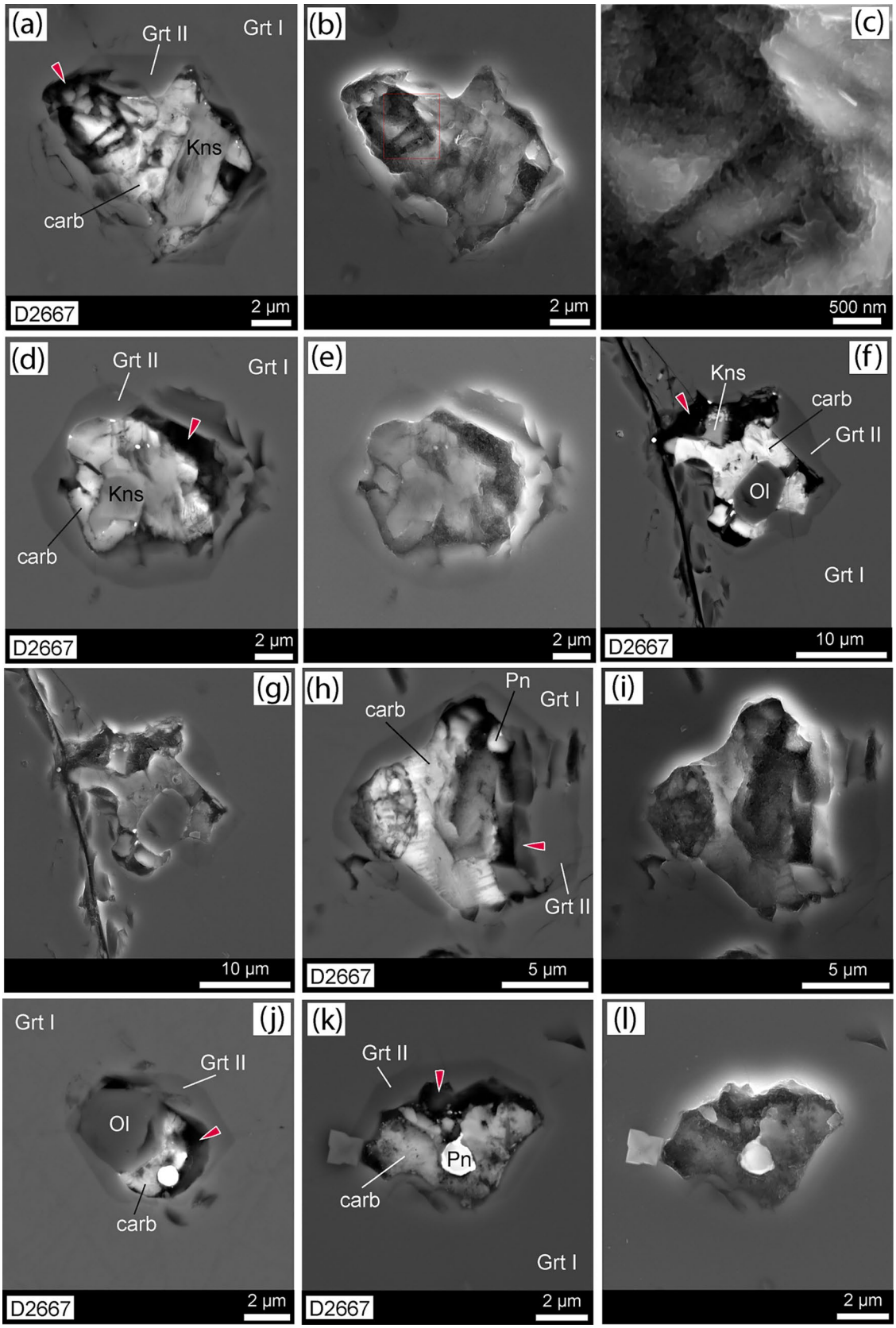

Fig. 3 Scanning electron microscope photomicrographs of experimental MSI in D2667 using either backscattered (**a**, **d**, **f**, **h**, **j**, **k**) or secondary (**b**–**c**, **e**, **g**, **i**, **l**) electrons. Red arrows show void space in the opened inclusions. Red square show region of MSI enlarged in the nearby photomicrograph. See text for explanation

After loading garnet fragments and graphite powder, capsules were closed by arc welding. Capsules were placed in an end-loaded piston cylinder apparatus, using a 1/2 inch-diameter pressure vessel and a "low-friction" and "dry" furnace assembly to embed the capsule. The assembly was formed by teflon foil, a NaCl outer sleeve, graphite heaters and MgO inserts. The presence of graphite in the experiment imposes an oxygen fugacity within the capsule of ≈ QFM-2 at the experimental pressure and temperature (Foley 2011). Capsules were first pressurized to the target P in 8–10 min, and then heated to the target temperature in 7–8 min. Pressure was converted from load on the piston, and temperature was controlled using type B thermocouples ($Pt_{94}Rh_6/Pt_{70}Rh_{30}$). Variations of P and T during the experiments with respect to the target values were ± 0.05 GPa and ± 2 ºC, respectively. Uncertainties in the measurement of P and T are ± 0.1 GPa and ± 10 ºC, respectively (Hermann and Spandler 2008). To explore the experimental behavior of MSI, a total of five experiments were conducted, varying P, T and run time between 4.0–4.5 GPa, 1000–1225 ºC and 30 min to 24 h, respectively (Table 1). Experiments were quenched by turning the power off, which cooled the samples to < 400 ºC in < 5 s while keeping the pressure. During both heating and quenching, P was manually adjusted to prevent P changes with T. After quenching capsules were opened, and garnet chips were recovered, mounted in epoxy, and polished until exposing and opening MSI for analysis.

Analytical methods

Natural MSI and experimental runs were examined using Jeol JSM-6610A, Tescan Mira3GMU FEG and QuemScan650F scanning electron microscopes (SEM), at the RSES (ANU), Czech Geological Survey (Prague) and CIC (Universidad de Granada), respectively. The composition of minerals in experimental inclusions was determined using a Cameca SX 100 (Masaryk University, Brno) and Jeol JXA-8200 (Universidad de Huelva, Spain) electron probe micro-analyzers (EPMA); both in wavelength dispersive mode, using an accelerating voltage of 15 kV, a beam current of 10–20 nA and a beam diameter of 1–5 µm. Natural and synthetic phases were used for calibration.

To compare with published data on bulk composition of natural MSI from Lh 332, we estimated the bulk major element composition of 9 experimentally treated MSI from D2667, with the same method used for the natural MSI (Kotková et al. 2021). A quantitative estimation of the volume % of phases was performed using the SigmaScan Pro 5 software. The bulk chemical compositions of inclusions were estimated considering the mineral proportions (vol. %), phase densities and average chemical compositions of phases in MSI calculated based on EPMA analyses.

Electron transparent foils were prepared for transmission electron microscopy (TEM) applying the site-specific focused-ion-beam (FIB) technique that allows cutting an electron-transparent foil from pre-selected areas of interest. The TEM foils were 15–20 µm wide, 10–15 µm deep and approximately 150 nm thick. Details of the technique are given in Wirth (2004, 2009). We conducted analytical and high-resolution transmission electron microscopy (ATEM, HRTEM) using a FEI Tecnai™ G2 F20 X-Twin at GeoForschungs Zentrum in Potsdam, operated at 200 kV with a field emission gun electron source. The TEM is equipped with a Gatan imaging filter (GIF Tridiem) allowing energy-filtered imaging. Analytical electron microscopy was performed with an EDAX X-ray analyzer equipped with an ultra-thin window. The X-ray intensities were measured in scanning transmission mode where the electron beam was scanned over a pre-selected area, thus minimizing mass loss during data acquisition.

Micro-Raman spectroscopy was conducted at the Department of Geological Science, Masaryk University, using a LabRAM-HR Evolution spectrometer (Horiba, Jobin–Yvon) with a Peltier-cooled CCD detector and Olympus BX-41 optical microscope in a confocal mode at room temperature. A diffraction grating with 600 grooves per millimeter was used. Raman spectra excited by 473 nm and 532 nm diode lasers in the range of 50(100)–4000(4200) cm^{-1} were collected from MSI under the surface of polished samples using 50 × (NA 0.75) and 100x (NA 0.9) objectives. The 473 nm laser spot diameter for the 50 × objective is ~ 0.8 µm. Acquisition times of 30–60 s per frame and 2 accumulations were used to improve the signal-to-noise ratio. Raman spectra were processed by the Seasolve PeakFit 4.1.12 software, providing precise band positions and deconvolution of overlapping bands by the Voigt function.

Results

Mineralogy and microstructures of experimental charges

Experimental charges show two types of reactions taking place during experiments. (i) On the one hand, in experiments D2667 and to lesser extent D2729 and C5636 (Table 1), edges of and veins across the starting garnet chips recrystallized to an assemblage of low Mg# olivine + low Mg#-high Ca garnet ± high Cr spinel (Supplementary Fig. 3a-b, Supplementary Table 1). Microstructures show that metasomatic replacements in veins start from the edges of the chips (Supplementary Fig. 3), hence metasomatic edges and veins are due to reaction with, and percolation of unintentionally added H_2O to some of the

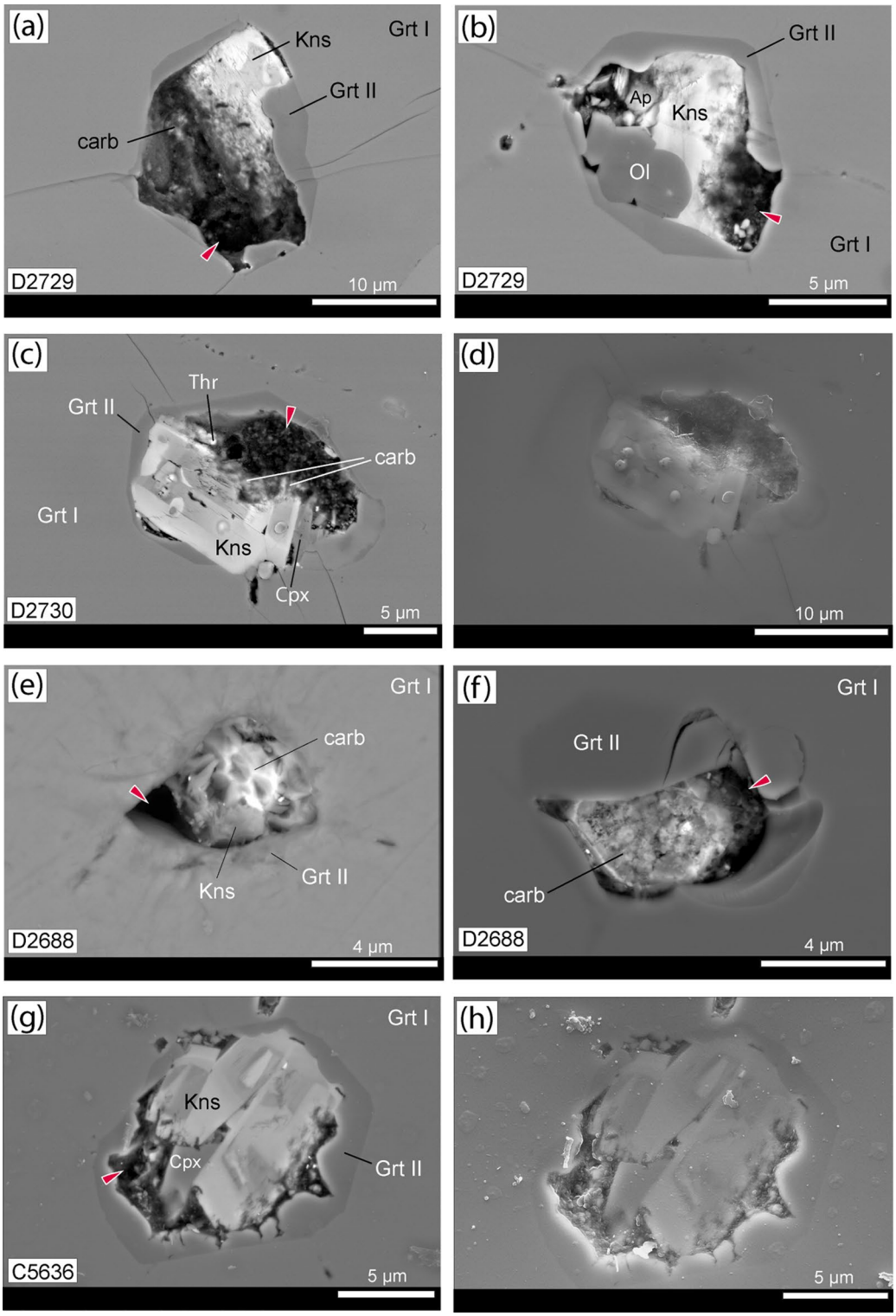

Fig. 4 Scanning electron microscope photomicrographs of experimental MSI in D2729 (**a**–**b**), D2730 (**c**–**d**), D2688 (**e**–**f**) and C5636 (**g**–**h**), using either backscattered (**a**–**c**, **e**–**g**) or secondary (**d**, **h**) electrons. Red arrows show void space. See also Supplementary Fig. 6

capsules. (ii) On the other hand, natural MSI recrystallized to a high Mg#-high Ca garnet fringe + void space + Ba-rich ternary carbonate + Ba-rich mica ± high Mg# olivine (Figs. 3–4, Table 2, see below). There are no traces of metasomatic veins emanating from the inclusions; and microstructures show no physical interaction between

Table 1 Conditions of, and mineral assemblages found in the conducted MSI rehomogenization experiments

Experiment label	*D2667	* D2729	D2730	D2688	*C5636
Run temperature (ºC)	1075	1075	1075	1225	1000
Run pressure (GPa)	4.5	4.2	4.0	4.5	4.0
Run time	24 h	63 min	31 min	24 h	24 h
No. studied/analyzed MSI	12/9 MSI	7/5 MSI	4/3 MSI	4/3 MSI	3/3 MSI
Major minerals in MSI	Grt II, Kns, carb, Ol	Grt II, Kns, carb, Ol, Cpx	Grt II, Kns, carb, Ol	Grt II, Kns, carb	Grt II, Kns, carb, Cpx
Accessory minerals in MSI	Pn, Thr, Gr, Mag	Ap, Pn, Gn	Thr	Pn, Aln, Pn	Aln, Py, Gn, Pn
Minerals in metasomatic veins	Grt III, Spl, Ol	Grt III, Ol			Grt III, Spl, Ol

Kns kinoshitalite, *carb* ternary carbonate, all other mineral abbreviations follow Whitney and Evans (2010)

*Experiments showing metasomatic replacement of starting garnet chips at edges and along fractures

garnet metasomatic replacements and recrystallized MSI (Supplementary Fig. 4). The mineralogy and/or mineral compositions of both types of reactions are systematically different. The mineralogy and mineral compositions of each particular type of reaction are similar among experimental charges. Hence microstructures, mineralogy and mineral compositions support that metasomatic replacements and recrystallized MSI represent two unrelated phenomena, one associated with unintentionally added H_2O to some capsules, the other related to the closed-system rehomogenization of primary former fluid inclusions trapped during the crystallization of garnet rims in Lh 332. Hereafter, this article only deals with the nature and significance of the experimentally treated MSI.

We have characterized a total of 30 MSI by SEM, 23 of which were analyzed by EPMA (Table 1). Four of the MSI in experiment D2667 have been studied via FIB-TEM to investigate the spatial relationships between phases underneath the exposed 2D surfaces. Fourteen MSI from D2667 and D2729 located underneath the exposed garnet surface were studied via Raman spectroscopy. Under the optical microscope, some MSI show irregular shapes and likely constitute decrepitated MSI (Supplementary Fig. 5e, quite similar to natural decrepitated MSI e.g. Figure 2e; and in contrast to natural undecrepitated MSI e.g. Figure 2f). Raman analysis confirms the presence of an aqueous fluid in these microstructures (Supplementary Fig. 7, Supplementary text A). In other cases, including MSI in the highest-T experiment, MSI have regular and close to negative crystal shapes and display no or slight signs of decrepitation, such as small offshoots (Supplementary Fig. 5b-d, f). The general microstructure, mineral assemblage and mineral compositions, are similar in all experimentally treated MSI: they systematically show a high Mg# and Ca garnet fringe at the boundary between MSI and the host garnet, an irregular void space (after polishing and exposing/opening the inclusions) next to the garnet fringe, and a heterogeneous Ca-Mg-Ba ternary carbonate and silicates kinoshitalite and/or high Mg# olivine towards the center of inclusions (Tables 1, 2; Figs. 3–4; Supplementary Fig. 6).

Experiment **D2667** was conducted at 1075 °C and 4.5 GPa. Temperature and P correspond to the highest P–T conditions calculated for the crystallization of the MSI-bearing garnet annulus. Fragments of host garnet in this experiment show frequent trails of secondary FI, sometimes in apparent contact with some MSI under the optical microscope (Supplementary Figs. 3c, 5a). However, high magnification SEM images show that the studied MSI often have regular and close to negative crystal shapes (Fig. 3), do not appear in contact with metasomatic veins or trails of secondary FI (Supplementary Fig. 4), and likely behaved as closed systems during the experiments.

Inclusions show a nearly continuous ≈0.5–5 µm thick fringe of garnet (hereafter Grt II; mineral abbreviations follow Whitney and Evans 2010), higher in Mg#, Ca, and lower in Fe, with respect to the host garnet (hereafter Grt I, Table 2). Both Grt I-Grt II interfaces and internal growth surfaces of Grt II, are euhedral to subhedral (Fig. 3; Fig. 5a–b, f–g, j). The central volumes of exposed inclusions are often occupied by an euhedral silicate crystal, often kinoshitalite (Kns) but sometimes olivine (Fig. 3a, d, f, j; Fig. 5b, f–g, j–k). A heterogeneous ternary Ca-Mg-Ba carbonate (carb) has grown in between Kns/Ol and Grt II, often attached to Kns/Ol and leaving a discontinuous empty space (hereafter void) with respect to the Grt II fringe (Fig. 3a, d, f, j; Fig. 5a–b, f–g, j–k). The surfaces of carbonate and Grt II covered with fine-grained olivine facing the void show botryoidal microstructures, suggesting the presence of a fluid (Fig. 3b–c, e, i, l; Fig. 5d, e). The systematic presence of an aqueous fluid within the void space after quenching has been confirmed by Raman spectroscopic analysis of unexposed inclusions (Supplementary Fig. 7, Supplementary text A).

The carbonate is highly heterogeneous in composition and microstructure, at the scale of 1 µm to hundreds of

Table 2 Mean compositions of minerals (wt%, 2σ values within brackets) present in experimental MSI of all runs, compared to those of sample lherzolite 332 in natural MSI or rock matrix

Experiment/rock	C5636	D2730	D2729	D2667	*MSI Lh 332●*	D2667	*MSI Lh 332●*	*MSI Lh 332●*	*MSI Lh 332●*	D2730	D2729	D2667	*Matrix Lh 332*
Mineral	Kns	Kns	Kns	Kns	*Kns*	carb	*Dol*	*Mgn*	*Nrs*	Ol	Ol	Ol	*Ol*
No. analyses	7	8	8	7	16	7	2	1	1	1	1	3	9
Vol.% (std dev)				5.4 (7.4)	30.1 (17.9)	26.3 (7.0)	16.3 (14.6)	7.0 (7.5)	6.0 (6.1)			6.3 (11.1)	
SiO_2	28.48 (5.14)	32.07 (5.37)	30.08 (4.18)	31.77 (4.25)	28.97 (1.77)	1.41 (1.82)	0.27	0.72	0.57	40.88	41.25	41.64 (1.34)	40.91 (0.33)
TiO_2	0.59 (0.37)	0.34 (0.29)	0.42 (0.28)	0.47 (0.42)	0.54 (0.81)	bdl	bdl	bdl	bdl	0.01	0.06	0.07 (0.11)	bdl
Al_2O_3	18.13 (1.42)	18.83 (2.91)	17.33 (3.65)	18.21 (2.87)	19.56 (0.99)	1.22 (1.21)	0.07	0.13	0.46	0.32	0.58	0.21 (0.56)	bdl
FeOt	2.72 (0.44)	2.47 (0.59)	2.47 (1.06)	2.13 (0.53)	3.99 (1.31)	1.42 (1.18)	2.70	3.50	1.07	3.63	5.20	3.92 (1.29)	9.72 (0.37)
FeO*													
Fe_2O_3*													
MgO	23.81 (2.32)	23.81 (1.88)	23.14 (1.75)	23.43 (2.47)	18.26 (1.48)	9.24 (2.75)	20.16	44.17	16.10	53.49	53.87	53.97 (2.04)	49.08 (0.23)
MnO	0.03 (0.03)	0.05 (0.06)	0.05 (0.05)	0.02 (0.03)	0.00 (0.02)	0.03 (0.11)	0.21	0.19	bdl	0.07	0.10	0.12 (0.09)	0.11 (0.00)
CaO	0.84 (1.63)	0.58 (0.87)	0.99 (2.96)	0.54 (1.61)	0.22 (0.29)	21.34 (6.07)	29.60	0.62	0.48	0.20	0.23	0.56 (0.90)	bdl
BaO	16.44 (6.08)	15.13 (8.45)	15.13 (4.69)	15.75 (5.19)	17.66 (2.67)	29.65 (8.29)	0.04	0.07	48.64	0.07	0.12	nd	bdl
Na_2O	0.61 (0.28)	0.50 (0.37)	0.35 (0.13)	0.40 (0.08)	0.54 (0.20)	0.17 (0.24)	0.07	bdl	bdl	bdl	0.01	0.06 (0.02)	bdl
K_2O	2.64 (1.98)	2.99 (2.50)	3.58 (1.52)	4.60 (1.75)	3.13 (0.92)	0.16 (0.29)	nd	nd	nd	bdl	0.01	nd	bdl
P_2O_5	0.04 (0.05)	0.04 (0.04)	0.21 (0.87)	nd	nd	nd	nd	nd	nd	0.02	0.08	nd	nd
Cr_2O_3	1.36 (0.89)	1.27 (0.66)	0.92 (0.37)	0.76 (0.24)	2.83 (0.96)	nd	bdl	bdl	bdl	0.15	0.17	0.12 (0.07)	bdl
V_2O_3	nd	nd	nd	0.07 (0.07)	0.07 (0.06)	nd	nd	nd	nd	nd	nd	nd	bdl
Sc_2O_3	nd	nd	nd	nd	nd	nd	nd	nd	nd	nd	nd	nd	nd
NiO	0.07 (0.06)	0.04 (0.06)	0.06 (0.04)	bdl	0.10 (0.14)	nd	nd	nd	nd	0.09	0.11	0.03 (0.06)	0.43 (0.05)
ZnO	0.07 (0.09)	0.04 (0.07)	0.03 (0.06)	nd	nd	bdl	0.07	bdl	0.09	bdl	0.03	nd	bdl
SrO	0.02 (0.00)	0.02 (0.01)	bdl	bdl	0.07 (0.08)	0.09 (0.19)	0.08	0.05	0.09	0.03	bdl	nd	bdl
F	nd	nd	nd	0.00 (0.00)	0.01 (0.04)	nd	nd	nd	nd	bdl	bdl	nd	nd
Cl	0.51 (0.60)	0.16 (0.04)	0.15 (0.06)	0.22 (0.16)	1.39 (0.76)	nd	nd	nd	nd	bdl	bdl	nd	nd
SO_3	0.13 (0.18)	0.08 (0.04)	0.07 (0.05)	nd	nd					0.01	0.01	nd	nd
CO_2						36.28 (5.18)**	47.07**	51.02**	32.61**				
H_2O	3.68 (1.21)**	1.67 (3.14)**	5.09 (6.94)**	3.82 (0.19)**	3.38 (0.29)**								
$0=F^-,Cl^-$				− 0.05	− 0.32								
Total	96.32 (1.21)	98.33 (3.14)	94.91 (6.94)	100.52 (1.05)	99.66 (1.67)	101.01 (5.13)	100.35	100.48	100.12	98.96	101.84	100.71 (1.18)	100.32 (0.61)
Mg#	94.0 (1.1)	94.5 (1.5)	94.4 (2.2)	95.6 (1.1)	89.1	92.5 (2.1)	93.0	95.7	96.4	96.3	94.9	95.8 (1.0)	89.3

Table 2 (continued)

Experiment/rock	C5636	*MSI Lh 332*•	C5636	D2730	D2729	D2667	D2688	*MSI Lh 332*•	*MSI Lh 332*•	C5636	D2730	D2729	D2667	D2688	*Lh 332*
Mineral	Cpx	*Cpx*	Grt II	Grt II	Grt II	Grt II	Grt II	*Grt II*	*Hbl*	Grt I, MSI	Grt I, MSI	Grt I, MSI	Grt I, MSI	Grt I, MSI	*Grt I*
No. analyses	1	3	3	5	6	5	1	1	8	4	6	6	5	6	50
Vol.% (std dev)		6.7 (11.0)				44.9 (11.3)		1.52 (4.6)	30.0 (17.2)						
SiO_2	52.50	54.19 (0.46)	42.93 (0.86)	41.32 (1.98)	43.81 (4.01)	42.86 (0.71)	41.57	42.35	44.06 (1.41)	40.38 (0.51)	40.94 (0.85)	41.12 (1.14)	42.36 (0.42)	40.36 (0.87)	41.83 (0.65)
TiO_2	0.18	0.03 (0.01)	0.16 (0.08)	0.19 (0.13)	0.27 (0.21)	0.20 (0.14)	0.08	bdl	0.09 (0.05)	0.32 (0.09)	0.30 (0.06)	0.33 (0.10)	0.31 (0.02)	0.31 (0.17)	0.29 (0.08)
Al_2O_3	2.43	10.15 (1.74)	21.62 (1.83)	23.32 (2.38)	21.21 (1.46)	22.42 (0.29)	23.13	23.65	16.63 (1.60)	20.83 (0.78)	21.58 (0.27)	20.97 (0.60)	21.30 (0.37)	20.92 (0.17)	21.08 (0.63)
FeOt	0.98	1.76 (0.38)	3.24 (0.23)	3.54 (0.62)	3.32 (0.44)		4.71			8.98 (0.20)	8.99 (0.21)	8.52 (0.20)		8.96 (1.13)	
FeO*						3.74 (3.04)		7.72	1.05 (0.75)				7.67 (0.44)		7.38 (0.76)
Fe_2O_3*						0.78 (0.43)		0.50	1.12 (0.89)				1.44 (0.21)		1.71 (0.68)
MgO	18.15	10.68 (0.09)	21.62 (1.57)	21.39 (1.55)	21.16 (3.93)	20.59 (3.24)	21.94	21.94	17.45 (1.19)	21.21 (0.72)	20.16 (0.48)	20.77 (0.57)	20.45 (0.49)	20.05 (2.38)	20.84
MnO	0.01	0.05 (0.05)	0.13 (0.06)	0.13 (0.07)	0.12 (0.06)	0.19 (0.18)	0.18	0.35	0.03 (0.03)	0.37 (0.08)	0.39 (0.09)	0.36 (0.06)	0.38 (0.03)	0.38 (0.03)	0.34
CaO	22.12	15.25 (1.25)	7.66 (3.07)	7.86 (2.72)	7.68 (3.70)	8.23 (2.44)	6.16	2.93	10.33 (1.42)	4.72 (0.08)	4.79 (0.25)	4.74 (0.17)	4.80 (0.07)	5.42 (3.08)	4.56
BaO	0.06	nd	0.37 (0.95)	0.04 (0.04)	0.33 (1.04)	nd	0.04	nd	0.64 (0.26)	0.05 (0.01)	0.02 (0.04)	0.03 (0.05)	nd	0.03 (0.02)	nd
Na_2O	0.82	5.83 (0.75)	0.10 (0.12)	0.04 (0.07)	0.05 (0.04)	0.03 (0.06)	0.01	0.03	4.56 (0.76)	0.03 (0.00)	0.04 (0.04)	0.03 (0.02)	0.04 (0.05)	0.02 (0.03)	0.04 (0.05)
K_2O	0.04	0.03 (0.02)	0.06 (0.14)	0.01 (0.01)	0.08 (0.28)	nd	0.01	nd	0.39 (0.23)	bdl	0.01 (0.01)	0.01 (0.00)	nd	0.01 (0.02)	bdl
P_2O_5	bdl	nd	0.11 (0.23)	0.11 (0.24)	0.19 (0.32)	0.04 (0.11)	0.07	bdl	nd	0.03 (0.03)	0.02 (0.02)	0.02 (0.02)	0.01 (0.02)	0.02 (0.03)	bdl
Cr_2O_3	1.00	2.24 (0.76)	2.43 (0.17)	1.74 (0.31)	1.81 (0.83)	2.14 (0.54)	1.44	0.76	2.08 (0.65)	2.55 (0.03)	2.40 (0.25)	2.23 (0.15)	2.45 (0.10)	2.33 (0.20)	2.42 (0.24)
V_2O_3	nd	nd	nd	nd	nd	nd	nd	nd	nd	nd	nd	nd	nd	nd	bdl
Sc_2O_3	nd	nd	nd	nd	nd	nd	nd	nd	nd	nd	nd	nd	nd	nd	nd
NiO	0.01	bdl	0.01 (0.02)	0.04 (0.05)	0.02 (0.03)	nd	bdl	nd	0.01 (0.03)	0.05 (0.05)	0.02 (0.02)	0.04 (0.02)	nd	0.01 (0.01)	nd
ZnO	0.01	nd	0.02	0.04 (0.04)	0.06 (0.01)	nd	0.03	nd	nd	0.04 (0.04)	0.07 (0.09)	0.03	nd	0.08	nd
SrO	0.01	nd	0.03 (0.03)	0.03 (0.05)	0.04 (0.04)	nd	bdl	nd	0.01 (0.02)	0.05 (0.03)	0.01 (0.02)	0.04 (0.03)	nd	0.02 (0.02)	nd
F	bdl	nd	bdl	bdl	bdl	nd	bdl	nd	0.12 (0.05)	bdl	bdl	bdl	nd	bdl	nd
Cl	0.01	nd	0.02 (0.01)	0.01 (0.01)	0.01 (0.01)	nd	0.01	nd	0.44 (0.60)	0.01 (0.01)	0.01 (0.01)	0.01 (0.01)	nd	bdl	nd
SO_3	0.01	nd	0.02	0.02 (0.02)	0.01 (0.02)	nd	bdl	nd	nd	0.04	0.02 (0.02)	0.02	nd	0.01 (0.01)	nd
CO_2															
H_2O									1.95 (0.18)**						
$0=F^-,Cl^-$									− 0.15						
Total	98.32	100.33 (0.61)	100.44 (0.54)	99.78 (2.02)	100.03 (2.31)	101.23 (1.34)	99.38	100.30	100.23 (1.28)	99.55 (1.13)	99.73 (0.82)	99.15 (1.71)	101.22 (0.95)	98.83 (0.84)	100.27 (1.06)
Mg#	97.1	91.5	92.2 (0.6)	91.5 (1.3)	91.8 (1.8)	89.1 (4.2)	89.3	82.7	93.8	80.8 (0.5)	80.0 (0.6)	81.3 (0.6)	80.3 (0.5)	80.0 (0.7)	80.6

Kns kinoshitalite, *carb* ternary carbonate, *Nrs* norsethite, all other mineral abbreviations follow Whitney and Evans (2010)

Repres. An. Representative analysis, *No.* number, *Vol.* volume, *std dev* standard deviation, *nd* not determined, *bdl* below detection limits

FeOt, Total Fe as FeO; FeO* and Fe_2O_3*, Fe concentrations based on calculated Fe^{2+}/Fe^{3+} ratios to maintain electrical neutrality

• Data from Kotkova et al. (2021)

**Based on stoichiometry

nanometers or even tens of nanometers. Brighter domains in BSE and TEM images are richer in Ba, whereas darker domains are richer in Ca-Mg (Fig. 3; Fig. 5a–c, k–l). None of the analyzed dark domains corresponds to a silicate glass. In some cases, the darkest regions correspond to MgO, either in contact with a high-Ba ternary carbonate or transitional to it through a high-Mg carbonate (Fig. 5k–l). The intimate contacts between the different compositional domains resemble graphic intergrowths (Fig. 5c, h), and/or intermingling between coexisting melts, and/or dendritic growth (Fig. 5k–l). Together with the presence of directional growth microstructures (Fig. 5b–d, g–h), all point to rapid growth of the carbonate.

Accessory minerals such as pentlandite, thorianite, graphite, MgO (periclase) and rare magnetite have also been observed. Pentlandite constitutes small anhedral to subhedral crystals a few µm in diameter (Fig. 3k). Thorianite forms polycrystalline aggregates ≈ 100 nm in diameter. Graphite forms euhedral flakes 150 nm thick and 1–2 µm long, in the void space in between Grt II and kinoshitalite, and partly included in carbonate; it appears partly amorphous in regions a few nanometers in size. Magnetite 500 nm in diameter appears included in ternary carbonate (Fig. 5l).

Experiments along a time series were conducted at 1075 °C, with 24-h (**D2667**), 63-min (**D2729**) and 31-min (**D2730**) run durations, and P somewhat variable between 4.5 and 4.0 GPa (Table 1). Most inclusions show regular and close to negative crystal shapes, with either tiny/small offshoots filled with Grt II (Fig. 3d, Fig. 4a, b) or small empty fractures/voids next to the inclusion (Fig. 3i, l; Fig. 4b; Supplementary Fig. 6b, d). The analysis of run products shows that all features described for the longest experimental run D2667 either develop in less than 1 h, and/or result from quenching (Figs. 3, 4a–d; Supplementary Fig. 6a-d). Inclusions in the shorter runs show zoned kinoshitalite crystals, with sharp contact between K-rich cores and Ba-rich rims (Fig. 4a, c; Supplementary Fig. 6c). Clinopyroxene is present in one studied inclusion of the shortest run D2730 (Fig. 4c).

Experiment **D2688** explored the behavior of MSI at 1225 ºC, c. 150–200 ºC above the crystallization T of the MSI-bearing garnet rim. Pressure was maintained at 4.5 GPa. Optical microscopy shows that most MSI have a regular negative crystal shape, with small offshoots in some of the inclusions (Supplementary Fig. 5b-c). Scanning electron microscope images show that even at these extreme T inclusions neither rehomogenized nor quenched to glass. They show mostly similar mineralogy and microstructures with respect to MSI in the experiment D2667 at 1075 ºC, including frequent regular close to negative crystal shapes, and the systematic presence of the Grt II fringe, void space, kinoshitalite and the ternary and heterogeneous Ca-Mg-Ba carbonate (Fig. 4e–f; Supplementary Fig. 6e–f).

Experiment **C5636** was conducted at 1000 ºC and 4.0 GPa. These values are slightly higher (T) or similar (P) to the lower P–T values calculated for the crystallization of the MSI-bearing garnet annulus. Even at this "low" temperature right at the peridotite + H_2O + CO_2 solidus (Foley et al. 2009), MSI recrystallized and mostly display similar mineralogy and microstructures to the experiment D2667, with regular negative crystal shapes and the presence of kinoshitalite/olivine crystals, a fringe of Grt II, void space and ternary carbonate (Fig. 4g–h; Supplementary Fig. 6g–h). The main differences with respect to previous experiments are the apparent lower proportion/absence of carbonate and presence of clinopyroxene in one out of three studied inclusions. Tiny empty voids appear next to some inclusions (Fig. 4h), whereas other show empty/partially empty offshoots (Supplementary Fig. 6g–h). Note, however, that shapes of inclusions in Supplementary Fig. 6g–h are similar to those of some natural MSI rich in Hbl, Kns and carbonates (Fig. 4b,c of Čopjaková and Kotková 2018; Fig. 4a,i of Kotková et al. 2021).

Comparison of mineralogy between experimental and natural MSI

Modal and mineral compositions of natural and experimentally treated MSI in Lh 332 have been compared, based on 2D FEG-SEM imaging of inclusions in experiment D2667, and EPMA mineral analyses from all runs (Tables 2, 3, Supplementary Table 2). Experiment D2667 has been used for modal analysis because (i) this experiment was conducted at P–T conditions well within those calculated for the crystallization of the MSI-bearing garnet annulus, and (ii) it presents the most robust results including a large number of studied inclusions, similarity between inclusions, and compositional homogeneity of minerals (except the carbonate).

Kinoshitalite in experimentally treated inclusions show much lower proportion and different composition (including dark cores in C5636, D2730, D2729) with respect to crystals in natural MSI, having higher Mg, Mg# (94–96 vs. 89), K, slightly lower BaO (15–16 vs. 18 wt %), Ti, Na, and lower Fe, Cl concentrations (Table 2). Although heterogeneous, the single ***carbonate*** incorporates all three components (Ca, Mg, Ba) of one- or two-component carbonates found in natural MSI (magnesite –Mg, dolomite –Ca, Mg, and norsethite –Ba, Mg). In addition, the single-phase carbonate contains 1–2 wt% of SiO_2, Al_2O_3, FeOt, and traces (≈ 1000–3000 ppm) of Na_2O, K_2O and SrO. The proportion of carbonates in natural versus experimentally treated MSI is roughly similar. ***Olivine*** has not been described in natural MSI; compared with matrix olivine of Lh 332, crystals in experimental inclusions are higher in Mg, Mg# (95–96 vs. 91) and lower in Fe, Ni. Abundant

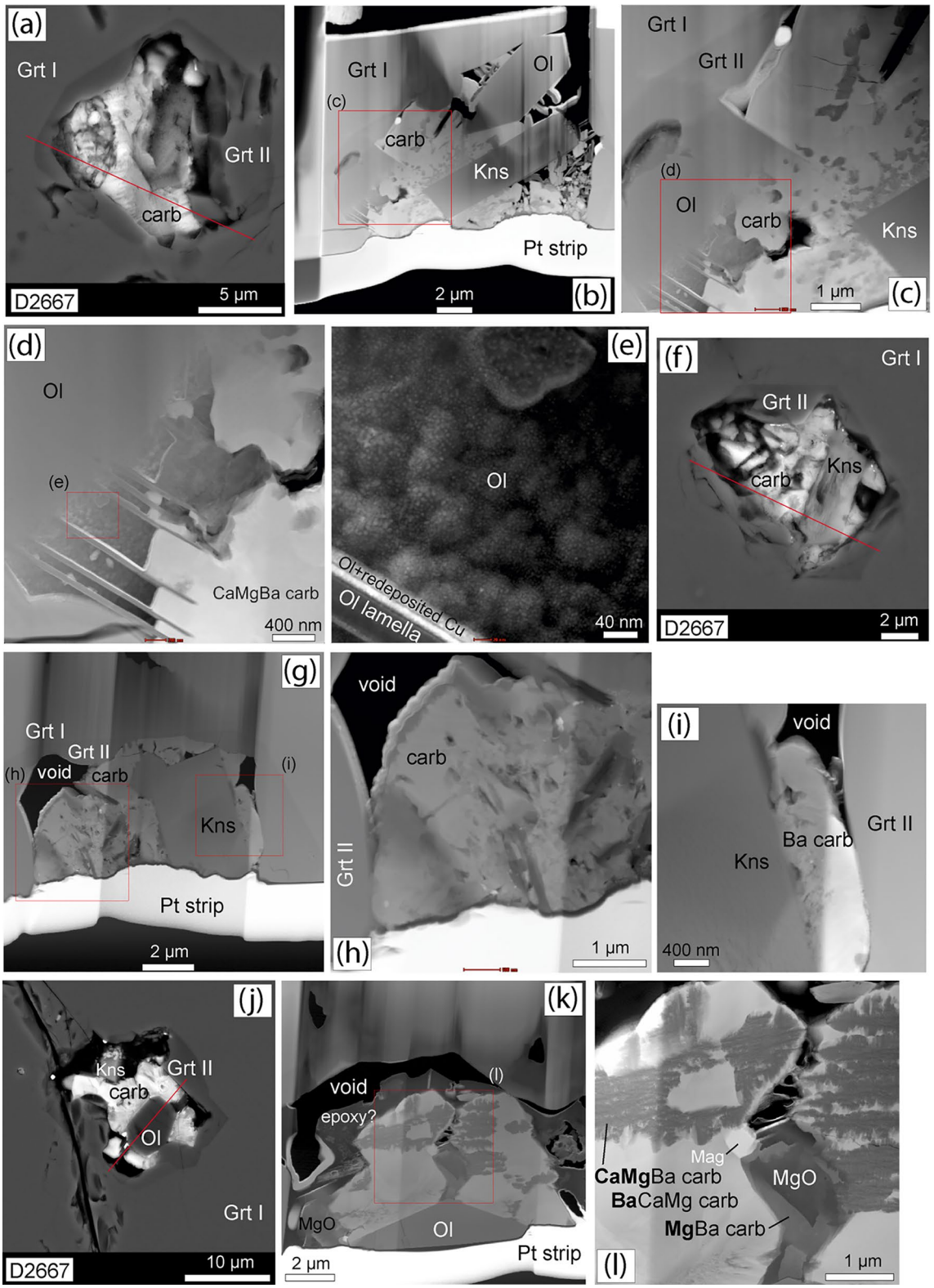

Fig. 5 Focused ion beam TEM images of experimental MSI in D2667. Red lines show the sliced 2D section perpendicular to the experimental charge surface and shown in nearby photomicrographs. Red squares show regions of the studied slice enlarged in the nearby photomicrograph. See text for explanation

hornblende present in natural MSI has not been observed in any experimentally treated MSI. ***Clinopyroxene*** has only been found in the lowest T (1000 ºC) and P (4.0 GPa) experiment C5636, and the shortest run D2730 (1075 ºC, 4.0 GPa, 31 min.). Clinopyroxene in C5636 is different from Cpx in natural MSI, showing much lower Al, Fe, Na and higher Ca, Mg, Mg#; it also shows higher Mg# with respect to Cpx in the matrix of Lh 332. Host ***garnet*** (Grt I) in the experimentally treated fragments, analyzed at c. 100 µm from MSI, has not changed composition with respect to natural garnet in Lh 332. In contrast, newly formed garnet fringes in MSI (Grt II) are systematically higher in CaO (6–8 vs. 4–5 wt%) and Mg# (89–92 vs. 80–81), and lower in Fe with respect to host Grt I. Rare garnet crystals observed within natural MSI from several peridotites (including Lh 332), have slightly different composition with respect to their host garnet (lower in Ca, Cr, Ti; Kotková et al. 2021). With respect to these rare garnet crystals, experimental Grt II is quite different in composition, being higher in Ca, Mg#, Cr and lower in Fe concentrations.

Overall, the above comparison indicates that silicates and carbonates present in natural MSI either disappeared or entirely recrystallized during experiments, and changes took place in < 1 h. The major changes in natural MSI during experiments were (i) the complete disappearance of abundant amphibole, (ii) the large decrease in the proportion and change in composition of kinoshitalite, (iii) the crystallization of olivine, (iv) the substitution of coexisting one- and two-component carbonates by a single ternary carbonate, (v) the appearance of a large proportion (c. 15–20%) of void space, and (v) the crystallization of a garnet fringe in between host garnet and void space. Apparently the starting accessory mineral assemblage, including pentlandite, thorianite and graphite, has not significantly changed; however, apatite seems less abundant, and monazite, scheelite have not been found in the studied experimental MSI.

Bulk compositions and redistribution of elements within MSI during experiments

Bulk compositions of natural and experimentally treated MSI in Lh 332 have been compared using experiment D2667, based on 2D FEG-SEM imaging, EPMA mineral analyses and phase densities (Table 3, Supplementary Table 2, and Kotková et al. 2021). It is important to notice that calculations regarding experimentally treated MSI consider all newly produced phases, including olivine and the garnet II fringe.

Bulk compositions of experimental MSI are lower in Na, K, H_2O, Cl and P, with respect to natural MSI (Table 3, Fig. 6, Supplementary Table 2). The rare presence of phosphates and lower phosphorus in experimental MSI can be

Table 3 Mean modal composition and bulk composition (vol% and wt%, respectively; 1σ values within brackets) of natural and experimental MSI from sample lherzolite 332 and experiment D2667, respectively

Experiment/Rock sample	*MSI Lh 332●*	**D2667**
No. studied MSI	9	9
Hornblende (vol. %)	29.96 (17.17)	0.00 (0.00)
Kinoshitalite	30.06 (17.92)	5.39 (7.44)
Garnet	1.52 (4.56)	44.90 (11.27)
Clinopyroxene	6.74 (11.02)	0.00 (0.00)
Olivine	0.00 (0.00)	6.30 (11.09)
Dolomite	16.30 (14.64)	0.00 (0.00)
Magnesite	6.97 (7.45)	0.00 (0.00)
Norsethite	5.95 (6.13)	0.00 (0.00)
Ternary carbonate	0.00 (0.00)	26.31 (7.00)
Ba feldspar	0.85 (1.36)	0.00 (0.00)
Periclase	0.00 (0.00)	0.36 (0.62)
Apatite	0.52 (0.99)	0.00 (0.00)
Graphite	0.00 (0.00)	0.00 (0.00)
Thorianite	0.29 (0.40)	0.00 (0.00)
Monazite	0.23 (0.50)	0.00 (0.00)
Pentlandite	0.07 (0.15)	0.31 (0.64)
Chalcopyrite	0.04 (0.13)	0.00 (0.00)
Galena	0.06 (0.19)	0.00 (0.00)
Scheelite	0.00 (0.00)	0.00 (0.00)
Unidentified accessories	0.00 (0.00)	0.12 (0.17)
Voids	0.43 (1.28)	16.31 (6.13)
Total	100.00 (0.00)	100.00 (0.00)
SiO_2 (wt. %)	26.14 (5.30)	28.45 (3.44)
TiO_2	0.19 (0.07)	0.14 (0.03)
Al_2O_3	12.39 (2.20)	13.87 (1.91)
FeO*	2.89 (0.40)	3.22 (0.30)
MgO	18.78 (1.59)	19.02 (3.17)
MnO	0.06 (0.02)	0.12 (0.02)
CaO	8.75 (3.30)	11.22 (1.36)
BaO	9.73 (4.81)	9.89 (2.56)
Na_2O	1.88 (0.74)	0.10 (0.03)
K_2O	1.03 (0.44)	0.32 (0.34)
P_2O_5	0.29 (0.49)	0.00 (0.00)
Cr_2O_3	1.61 (0.31)	1.25 (0.19)
V_2O_3	0.03 (0.01)	0.03 (0.00)
NiO	0.04 (0.02)	0.01 (0.00)
ZnO	0.04 (0.01)	0.02 (0.01)
SrO	0.05 (0.02)	0.03 (0.01)
ThO_2	0.48 (0.50)	0.00 (0.00)
UO_2	0.32 (0.40)	0.00 (0.00)
La_2O_3	0.15 (0.27)	0.00 (0.00)
Ce_2O_3	0.08 (0.13)	0.00 (0.00)
Nd_2O_3	0.00 (0.01)	0.00 (0.00)
F	0.04 (0.02)	0.00 (0.00)
Cl	0.65 (0.21)	0.01 (0.02)
S	0.07 (0.11)	0.17 (0.34)

Table 3 (continued)

Experiment/Rock sample	*MSI Lh 332*•	**D2667**
Fe	0.05 (0.08)	0.16 (0.33)
Pb	0.12 (0.34)	0.00 (0.00)
Ni	0.04 (0.07)	0.17 (0.35)
Cu	0.02 (0.06)	0.00 (0.00)
CO_2	12.62 (5.50)	11.56 (2.59)
H_2O	1.62 (0.36)	0.22 (0.28)
O = – F,Cl	-0.16 (0.04)	0.00 (0.00)
Total	100.00 (0.00)	100.00 (0.00)
ASI	0.72 (0.40)	0.67 (0.12)
Mg#	92.0 (1.2)	91.2 (1.1)

• Data from Kotkova et al. (2021)

*Total Fe as FeO

reasonably attributed to the dissolution of phosphates into the carbonatitic melt. It is remarkable that all other components with lower concentrations typically constitute brines. For instance, some high-density fluid inclusions found in fibrous diamonds (implying P–T conditions of genesis similar to the studied inclusions: P ≥ 4.5 GPa at T of 1000–1100 ºC) correspond to saline Cl-K-Na-H_2O fluids (e.g. Tomlinson et al. 2006; Klein-BenDavid et al. 2007; Weiss et al. 2015). Raman spectroscopy has confirmed the presence of H_2O within unexposed experimental inclusions, hence it is reasonable to assume that before polishing and opening, the void space of experimental MSI was filled with a high-density saline H_2O-Na-K-Cl fluid. Mass balance calculations considering a likely composition for this brine (Supplementary text B) provide good fits between bulk concentrations of H_2O, Na_2O, K_2O and Cl in natural and experimental inclusions (Fig. 6). Overall, calculations indicate that all/most Si, Al, Fe, Mg, Ti, Ca, Ba and CO_2 have been concentrated in new experimentally produced minerals garnet II fringe, carbonate, kinoshitalite and olivine, whereas all/most volatiles (H_2O, Cl) and alkali metals (Na, K) likely segregated into a fluid present within uncovered experimental inclusions (Fig. 7). Except for Ba, volatiles and alkali metals, all major components of hornblende and most of the starting kinoshitalite were transferred to garnet II (compare columns of natural hornblende + kinoshitalite vs. columns of experimental garnet II, Fig. 7). Barium and CO_2 present in most/all of starting kinoshitalite and carbonates have been transferred to the experimental ternary carbonate. Micro-Raman analyses and mass balance indicate that CO_2 is not present in the experimental fluid (Supplementary text B).

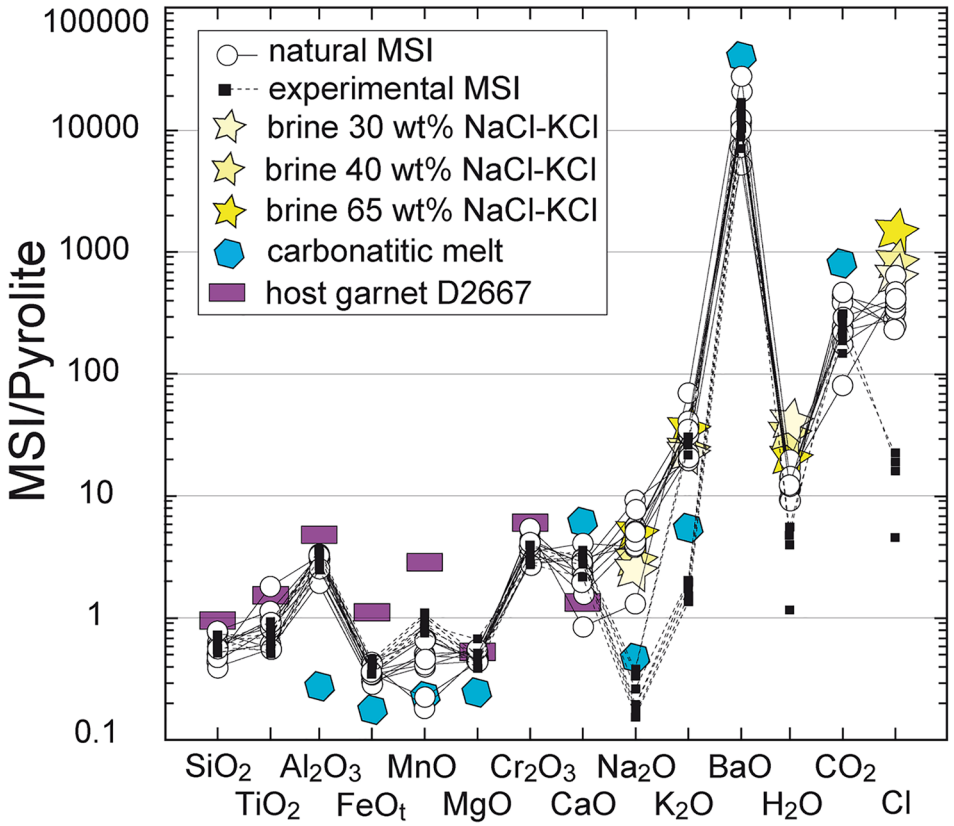

Fig. 6 Comparison of calculated major element bulk compositions of natural (white circles) and experimentally treated MSI (black squares) in lherzolite 332, normalized to the pyrolite (McDonough and Sun 1995). The diagram also includes the normalized compositions of the host garnet in experiments nearby the inclusions (purple rectangles), the ternary carbonate found in experimental MSI (blue hexagons), and the calculated Na_2O, K_2O, H_2O and Cl bulk composition of experimental inclusions assuming the presence within inclusions of a brine with different salinity (yellow stars). See text for explanation

Discussion

Behavior of MSI during experimental versus natural P–T-time paths

Before discussing the experimental results, it is worth comparing the behavior of inclusions trapped in garnets of lherzolite 332 during both experimental (red arrows, Fig. 8) and natural (green arrows) P–T-time paths. The endpoint of slow cooling and exhumation in nature and starting point of experiments (point 0: 25 ºC, ambient P), is a typical and well-preserved MSI found in garnet (Fig. 8a), made of hornblende, kinoshitalite and carbonates (Fig. 2f; Kotková et al. 2021). To prevent from decrepitation of, and mass loss from inclusions during experimental heating, capsules were first pressured cold in c. 10 min to maximum P recorded by the MSI-bearing garnet annulus, 4.5 GPa (point 1: 25 ºC, 4.5 GPa), similar to or slightly above pressures at which inclusions were trapped (P_{trap}, Fig. 8b; see above). This ensured that internal pressures in experimental inclusions (P_{int}) were always lower than external experimental pressures (P_{ext}) exerted on host garnet fragments, except at the end of the heating stage, when experimental T reaches the temperature of entrapment (T_{trap}), $P_{int} \leq P_{ext}$, and the experiment starts (Fig. 8b; and point 2: 1075 ºC, 4.5 GPa). Decrepitation necessarily occurs when $P_{int} >> P_{ext}$ and host garnet breaks, which cannot be the case in these experiments. Similarly, to preserve phases and compositions present in inclusions at target experimental P–T, quenching was conducted by extremely rapid cooling (in seconds) while maintaining the experimental P_{trap} (Fig. 8, point 3: 25 ºC, 4.5 GPa). This ensured that $P_{int} < P_{ext}$ at any time during the sudden drop in T and quenching.

Green arrows in Fig. 8 show the P–T path of peridotites during cooling and exhumation, after MSI entrapment in garnet at P–T of rim crystallization (continuous line from Haifler et al. 2024; discontinuous line from Haifler and Kotková 2016, based on work in the Eger Crystalline Complex outcroping at c. 60 km SW of T-7 borehole). In contrast with experimental cooling that takes place in seconds and with $P_{ext} > P_{int}$, natural cooling and exhumation occurred in timeframes of $\geq 10^5$–10^6 yrs (e.g. Závada et al. 2021). During this long period of time and extensive P–T journey, (i) trapped fluid likely reacted with host garnet (Fig. 8g), as indicated by the formation of Grt II fringes and their mass coming from starting kinoshitalite and hornblende (Fig. 7); (ii) P_{int} progressively became larger than P_{ext} (Fig. 8h) such that, at some critical value of ΔP ($= P_{int} — P_{ext}$), a proportion of the inclusions decrepitated (Fig. 2e, g; Supplementary Fig. 1b-d), e.g. based on a hypothetical isochore P_{int} may have been higher than P_{ext} by c. 2 GPa (point 4: 1000 ºC, 2 GPa); (iii) fluid crystallized; and (iv) minerals within

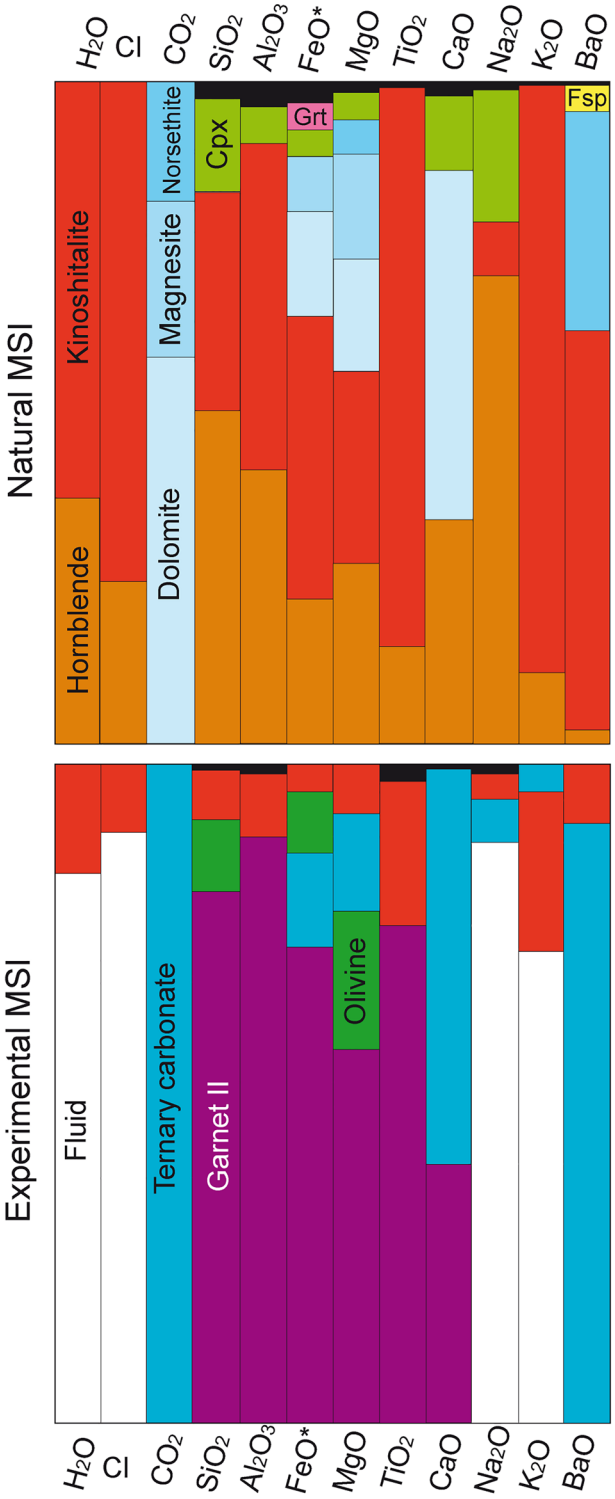

Fig. 7 Distribution of major elements among phases in natural and experimental MSI from mass balance calculations. Black color indicates other minerals than those specified in the figure. Mineral abbreviations follow Whitney and Evans (2010)

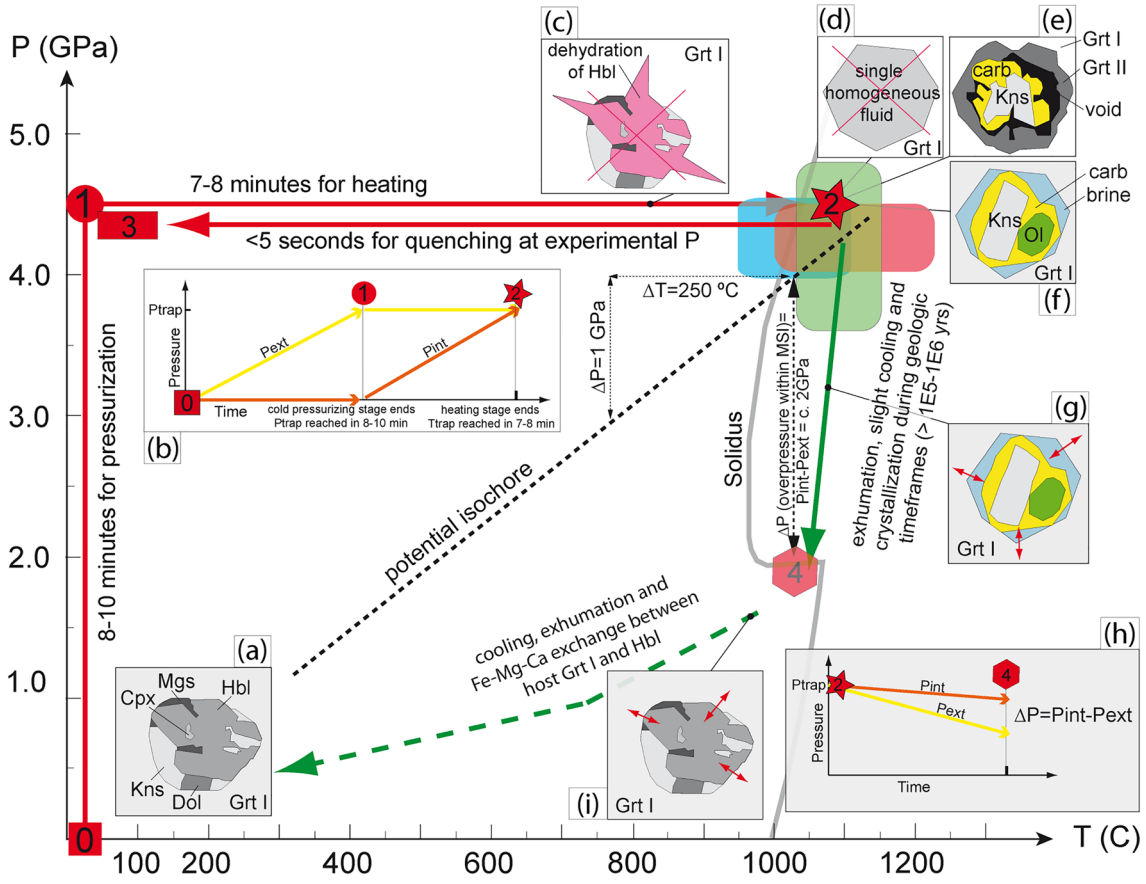

Fig. 8 Pressure–T diagram showing the behavior of inclusions trapped in garnets of lherzolite 332 during both experimental (red arrows) and natural (green arrows; after Haifler et al. 2024) P–T-time paths. Red rectangle shows the range of P–T experimental conditions used in this work. Green rectangle shows the range of calculated peak P–T conditions by Medaris et al. (2015) for pyroxenite and peridotites of the ultramafic T-7 borehole body. Blue rectangle shows the range of calculated P–T conditions by Haifler et al. (2024) for the crystallization of the MSI-bearing garnet rims. Insets (**a**) to (**i**) refer to situations of experimental (white background) and natural (light-grey background) MSI at different stages along the P–T-path. The oxidized solidus of the peridotite + H_2O + CO_2 system is from Foley et al. (2009). See text for explanation

inclusions reacted/equilibrated with host Grt down the exhumation and cooling path, e.g. Hbl-host Grt Fe–Mg-Ca exchange reactions (Fig. 8i).

The comparison of red and green P–T-t paths shows that decrepitation and fluid loss from MSI is much more likely during the slow natural cooling with $P_{int} > P_{ext}$, than during 24-h experiments where $P_{ext} \geq P_{int}$ and very rapid cooling with $P_{ext} > P_{int}$.

Inferences from microstructures and mineral compositions of experimental MSI

All experiments produced quite similar and robust results in terms of microstructures, mineralogy and mineral compositions, including run D2667 conducted within the estimated P–T conditions of entrapment. Contrary to Malaspina et al. (2006), however, our experiments were not able to rehomogenize the MSI, in the sense of producing a single fluid phase at the experimental conditions and freezing this phase into a solid (glass) upon quenching (Fig. 8d). Hence the results do not apparently support our starting hypothesis that MSI represent a trapped single solute-rich liquid.

Experimentally treated MSI are commonly subhedral to euhedral and similar in size to the natural MSI. Optical microscopy shows small offshoots and, less frequently, haloes of small fluid inclusions around several of the studied inclusions. These decrepitation microstructures seem to appear under SEM as empty fractures or voids (c. 1–3 µm across) at 5–10 µm from the euhedral MSI, and tiny offshoots (c. 1–2 µm long) on the edges of inclusions filled with Grt II (Figs. 3–4; Supplementary Fig. 6). About 30–40% of the natural Lh 332 MSI show clear decrepitation microstructures as well, showing offshoots and haloes partially filled with magnesite, graphite, kinoshitalite, Ba-feldspar and rare NaCl (Fig. 2g; Supplementary Fig. 1b-d). Given that

experimental decrepitation is unlikely (Fig. 8b), decrepitation microstructures in experimental MSI can be inherited from the starting MSI, with or without loss of material during natural decrepitation. Nevertheless, similar mineralogy and mineral proportions in decrepitated versus undecrepitated natural MSI suggests that mass loss was not significant.

With respect to the natural inclusions, experimental MSI entirely (re)crystallized to: (i) a much drier silicate component; and (ii) a single but more complex carbonate component that has sequestered most Ba of the inclusion; with (iii) the presence of an irregular empty space (voids) that Raman spectroscopy, mass balance and microstructures identify as a volume occupied by a saline aqueous fluid dissolving most of the alkalis, F and Cl.

Large and euhedral-to-subhedral garnet II fringes (e.g. Figures 5a–b, j–k) indicate that they crystallized during the experiments and not upon quenching. Garnet II shows different composition and microstructure/location with respect to rare garnet crystals found within the natural inclusions (Table 2; see Kotková et al. 2021). Mass balance (Fig. 7) unequivocally indicates that a large proportion of Si, Al, Fe, Mg, Ti and Ca within the natural MSI goes back to form garnet during rehomogenization at trapping P–T. This implies that if the studied inclusions have not leaked, trapped fluids and host garnet reacted upon slow decompression/cooling to form ferromagnesian minerals, including amphibole (Fig. 8g). Experiments are just reversing that reaction. Differences in Mg# and Ca between host Grt I and Grt II are possibly due to the transfer of Mg-Ca from host garnet to Hbl during exchange reactions upon slow cooling (Fig. 8i; Ravna 2000; Alonso-Pérez et al. 2009). This exchange is not reversed during quick 24-h experiments (Fig. 8e), and may explain higher Mg# in MSI compared to host garnets (Supplementary Fig. 8a).

Large and euhedral kinoshitalite and olivine crystals indicate that these minerals were stable at experimental P–T and did not crystallize upon quenching. Olivine has not been described within natural MSI. Kinoshitalite shows much lower proportion, different composition and mostly different location within experimental inclusions, with respect to crystals in natural MSI (Table 2; compare Figs. 3–4 with Fig. 2f–g; Supplementary Fig. 1a, c; and with Čopjaková and Kotková 2018 –Fig. 4, and Kotková et al. 2021 –Fig. 4). These observations indicate that olivine and the Ba-mica (re) crystallized during the experiments, and were stable at near-peak conditions. The presence of kinoshitalite at 1225 °C (and 4.5 GPa) is remarkable and indicates that Ba mica is stable to such very high temperatures. Previous studies have also observed that phlogopite is a stable phase at 4.0–4.6 GPa and 1200–1240 °C in K-enriched ultramafic systems (Konzett et al. 1997).

It is illustrative comparing the microstructures of the ternary carbonate with those of Kiseeva et al. (2012), who experimentally studied melting in carbonate–silicate mafic systems at UHP conditions. Quenching of those experiments shows the coexistence of silicate and carbonate melts; the silicate component appears as a glass, whereas the carbonate component is heterogeneous and patchy compared to carbonate crystals formed at subsolidus conditions. This indicates that in the current experiments there was no silicate melt present at experimental conditions; instead, most silica partitioned into silicates garnet II, kinoshitalite and olivine (Table 2, Fig. 7). It also indicates that the ternary carbonate likely represents a carbonate melt at the experimental conditions, with a small silicate component (Table 2), and into which most of the Ba partitioned. Microstructures and the heterogeneity of the ternary carbonate suggest rapid crystallization upon quenching of a melt (Fig. 5a–d, f–h, j–l). The location of the solidus (Fig. 8) requires that the carbonate melt had some H_2O dissolved (see also Kiseeva et al. 2012), that possibly exsolved upon quenching and solidification into sub-micron fluid inclusions. The large and mostly single and irregular space defining the voids, and microstructures present on the surface of carbonate and garnet II, suggest however that the carbonate melt was already coexisting with a fluid at the experimental conditions.

Significance of the studied multiphase solid inclusions

The experiments have not rehomogenized the natural MSI to a single fluid (Fig. 8d), but instead have produced a solid silicate assemblage (garnet II ± kinoshitalite ± olivine) apparently coexisting with a Ca-Mg-Ba carbonatite melt and a saline Na–K-Cl-F-bearing aqueous fluid (Fig. 8e). Below we provide some explanations of these results and discuss their plausibility.

Loss of fluids from the inclusions impeded rehomogenization

Inclusions may have leaked during natural decrepitation. A significant proportion of the natural inclusions show microstructural signs of decrepitation (Fig. 2c, e, g, Supplementary Fig. 1b–c; Fig. 8h). Even well preserved inclusions lacking clear signs of decrepitation (Fig. 2f) may have leaked, and fractures healed at high T afterwards. This would explain that decrepitated and undecrepitated inclusions show similar phase assemblages and mineral proportions, with abundant kinoshitalite, hornblende and carbonates. Hence we cannot discard that experiments started with inclusions that already lost some of the originally trapped material, which prevented inclusions from rehomogenization to a single fluid at trapped P–T.

Another possibility is that upon heating, hornblende decomposes and produces a free fluid phase that

instantaneously escapes from inclusions before reaching experimental target T (Fig. 8c). This could explain both failure of inclusion to rehomogenize and the missing H_2O-Na-K-Cl-F component of experimentally treated exposed inclusions. However, the cold pressurization of inclusions to maximum pressures recorded by the MSI-bearing garnet annulus (4.5 GPa), before any heating occurs, guarantees that Hbl did not decompose with $P_{int} > P_{ext}$, and in fact that $P_{ext} \geq P_{int}$ at all times. Hence inclusions did not likely decrepitate during the experiments (Fig. 8b), and neither physical paths were created upon experimental heating, nor there was any driving P gradient for a fluid to leave the inclusion (Fig. 8c). This is supported by the presence of an aqueous fluid within uncovered experimental inclusions (Supplementary Fig. 7). We cannot discard, however, that some small fraction of the fluid migrated during experiments into the vicinity of inclusion to fill decrepitation microstructures inherited from the natural MSI, as suggested by Raman analysis around experimental MSI (Supplementary Fig. 7, Supplementary text A).

It is also possible that fluid was lost from inclusions due to volume diffusion through garnet, associated with hypothetical chemical potential gradients present between inclusions and host garnet/rock matrix. Short-duration experiments of 30 min to 1 h, with in practice no diffusion of hydrogen through garnet, show similar microstructure (e.g. voids), mineralogy, and mineral compositions with respect to 24-h experiments. This, together with hydrogen diffusion calculations (Supplementary text C), suggests minimum modification of inclusions during the experiments. However, calculations show that aqueous fluid may have been lost from natural inclusions after entrapment and before crystallization, if appropriate chemical potential gradients between inclusions and garnet/rock matrix were present at that time. We cannot discard that this may have prevented inclusions from rehomogenization. The observation that studied decrepitation products of natural MSI correspond to either solid phases or empty cavities (Supplementary text A) suggests the loss of H_2 or H_2O from the natural MSI.

Trapped fluid(s) produced metasomatic olivine and mica via reaction with host garnet

Microstructures suggest that garnet trapped two coexisting and immiscible fluids represented by a carbonatite melt and a Na-K-Cl-F aqueous fluid or brine (Fig. 8f), but we cannot discard that there was only a hydrous carbonatite melt that exsolved the brine upon quenching. Experiments indicate that olivine with high-Mg# (≈ 95–96) and kinoshitalite are stable at trapped P–T conditions, and suggest that both minerals coexisted with the matrix fluid(s). Thus olivine and kinoshitalite may represent reaction products between fluid(s) and host garnet at trapped P–T.

High-Mg# olivine is a typical metasomatic product formed during the interaction of peridotite and carbonatitic melt (e.g. Gervasoni et al. 2017). Kinoshitalite has not been described neither in the matrix nor as single mineral inclusions in garnets from peridotites. Crystallization of Ba-rich metasomatic phlogopite in an Al-poor rock (3.4 wt% Al_2O_3, Medaris et al. 2015) occurred at the contact between the only Al-rich mineral in the rock, garnet (21 wt% Al_2O_3, Table 2), and the Ba-rich fluid. A potential reaction for the generation of metasomatic kinoshitalite, pointing to the key role of the carbonatitic melt loaded in Ba (e.g. Li et al. 2020), is the following: $BaCO_3$ (in carbonate melt) + garnet = Ba-mica + $CaCO_3$ (in melt) ± olivine. Thus kinoshitalite forms where the key ingredients meet: Ba, alkalis and H_2O from the fluid(s), and Si, Al from garnet. Chromium is not mobile in the fluid(s), hence high Cr contents in the Ba-mica were inherited from the high-Cr hosts garnets (Table 2), and suggest the metasomatic reaction above. Positive correlation between Cr in host garnet vs. Cr in kinoshitalite ($R^2 = 0.80$; Supplementary Fig. 8b–c) and mass balances (Fig. 7) also support this hypothesis.

The decrease in P and T during exhumation produced the microstructural reorganization of mass within the MSI and host garnet at the boundary, which included, at least, the following steps. (a) The reaction of fluid(s) with host garnet (Fig. 8g) that eventually resulted in the crystallization of ferromagnesian phases e.g. amphibole (Fig. 7). The absence of olivine and a free fluid phase in natural MSI, coupled with the absence of amphibole in the experimental MSI, can be explained with a reaction such as olivine + garnet + brine = amphibole. (b) The increase in the proportion of kinoshitalite. (c) The crystallization of carbonatite melt into one- and two-component carbonates, with the previous transfer of Ba from carbonatite melt to kinoshitalite (Fig. 7). (d) The exchange of Fe, Mg and Ca between host Grt and crystallized minerals in inclusions e.g. hornblende (Fig. 8i). We note that silicate followed by carbonate crystallization of the MSI occurred at c. 1100 °C and 2 GPa (Haifler et al. 2024).

These potential metasomatic and exchange reactions between trapped fluid(s) and garnet, imply that calculated bulk compositions of crystallized MSI should not be directly equated to the composition of a fluid present in the matrix coexisting with the crystallizing host mineral. Instead, experiments indicate that these may represent a combination between the composition of trapped fluid(s) and the mineral host (see also Stöckhert et al. 2001). Metasomatic and exchange reactions between trapped fluid and host mineral may be particularly important in the cases when the P–T conditions of entrapment are extreme, as there is a large

T(-P) interval between entrapment and crystallization of fluids/end of exchange reactions.

It is intriguing that separate inclusions of former carbonatite melt and brine have not been observed in the studied natural garnets, as in other cases where the coexistence of two immiscible fluids has been documented (e.g. Cesare et al. 2015). It could be argued that both fluids, derived from the same source (Px 256) and produced upon evolution of a single carbonate–silicate fluid (see below), percolated together along the same physical paths due to surface energy requirements. Alternatively, the aqueous fluid within experimental inclusions confirmed by Raman spectroscopy might have exsolved from the carbonatite melt upon quenching.

Distribution of barium in brine, carbonatite melt and mica at 4.5 GPa and 1075 °C

An important observation from these experiments is the stability of Ba-rich mica at P–T conditions of 4–4.5 GPa and 1000–1225 °C, in the presence of a carbonatite melt and possibly an aqueous saline fluid. These observations have implications for the partitioning of Ba between fluids and solid residue at subarc depths, and hence for the transfer of these elements between Earth's surface and mantle geochemical reservoirs.

Mineral analyses and mass balance indicate that at 4.5 GPa and 1075 °C, Ba is largely compatible in both carbonatite melt and mica with respect to saline aqueous fluid. Barium strongly partitions into the carbonatite melt and, to a lesser extent, into the mica; very minor Ba seems to enter the saline aqueous fluid (Fig. 7). Electron probe microanalyses provide a partition coefficient of ≈ 2.5–3 between carbonatite melt and mica. Although this value has to be taken with some caution due to the heterogeneity of the carbonatite melt quenched product, the results do indicate that Ba is more compatible in carbonatite melt than kinoshitalite. A high affinity of Ba for carbonatite melt compared to silicate melts of a variety of compositions, and particularly for H_2O-bearing systems, has been established in experiments at 1–3 GPa and 1150–1260 °C (Martin et al. 2013). Considering the main phases present within the inclusions (carbonatite melt, mica, olivine, brine), we suggest that the carbonatite melt might also be the main carrier of other incompatible elements such as Sr, Th, U and Pb. This is supported by positive correlations between CO_2 and Th, U, Ba, LREE using calculated bulk compositions of the natural MSI (Kotková et al. 2021).

Origin of the multiphase solid inclusions

Medaris et al. (2015) have concluded that the pyroxenite-harzburgite 256 association resulted from the infiltration of a subduction-related hydrous silicate melt (represented by pyroxenite 256), that produced modal metasomatism of harzburgite 256 and cryptic metasomatism of all other analyzed peridotites. Čopjaková and Kotková (2018) and Kotková et al. (2021) have further inferred that the infiltrating metasomatic agent was a silicate-carbonate liquid, by describing and analyzing MSI present in garnets of pyroxenite 256 and peridotites.

The experimental remelting of the inclusions sheds further light on the metasomatic process described above. There is no evidence of any residual hydrous silicate melt component in the remelted MSI, which instead host a carbonatite melt with a small silicate component ± a brine. A key feature of these inclusions is the extreme enrichment of Ba (Kotková et al. 2021). Barium concentrations of either granitic melts derived from anatexis of metasediments at subarc depths (Hermann and Rubatto 2009; Stepanov et al. 2016) or kimberlites (Giuliani et al. 2020) range between ≈500–3,000 ppm, which agrees well with the Ba concentration in pyroxenite 256 of ≈ 1,500 ppm (Kotková et al. 2021). However, these concentrations are much lower than those in the studied MSI: Ba ≈ 8,500–19,000 ppm in inclusions of pyroxenite 256 and adjacent harzburgite 256; Ba ≈ 16,000–100,000 ppm in inclusions in more distal metasomatized peridotites (Kotková et al. 2021). There is a roughly positive correlation ($R^2 = 0.55$) between Ba concentrations in MSI and distance to pyroxenite 256 (Fig. 1). Our study shows that about 90% of Ba is hosted in the carbonatite melt at conditions of entrapment (Fig. 7). The enormous Ba concentrations in these MSI imply that the fluid(s) in the MSI must have been trapped after consuming most of the originally percolating metasomatic fluid, in order to reach Ba concentrations one to two orders of magnitude higher compared to those of subarc granitic melts or kimberlites. This agrees well with a residual character of the MSI and points to a distillation process during the metasomatism (Kotková et al. 2021). Assuming a starting Ba concentration of 1,500 ppm in the intruding metasomatizing hydrous melt, and perfect incompatible behavior of Ba, consumption of c. 82–92% of the original mass is required to produce the concentrations of Ba in MSI in garnets of pyroxenite and harzburgite 256, and of c. 91–99% in the case of MSI in garnets of peridotites further from pyroxenite 256. This indicates that most (≈ 82–92%) of the intruding hydrous melt was already consumed in the pyroxenite vein before producing the MSI in the garnets of pyroxenite and harzburgite 256. This occurred by direct crystallization of the melt into the pyroxenite minerals (Medaris et al. 2015; Kotková et al. 2021) and/or by reaction of the melt with, and metasomatism of the host peridotite, where most of the Si, Al, Ca and Na component of the initial hydrous silicate-carbonate melt was used to produce garnet and clinopyroxene of pyroxenite 256 (see

Manning 2004; Malaspina et al. 2006; Arai and Ishimaru 2008). Our experiments suggest that residual products of this crystallization and/or metasomatism were a carbonatite melt ± a saline aqueous fluid. This explains the absence of a silicate melt component in the remelting experiments: it was already consumed before entrapment of inclusions. Percolation of these residual fluids following the model proposed by Kotková et al. (2021) produced the cryptic metasomatism of the neighboring peridotites, with the crystallization of rims of garnet and entrapment of the MSI.

This scenario agrees well with experiments by Förster et al. (2019) where melting of subducted sediments at 4 GPa, 1000 °C produced a chlorine-bearing hydrous carbonated silicate melt. The interaction of these melts with a peridotite layer also at 4 GPa, 1000 °C produced a reaction zone consisting of clinopyroxene, orthopyroxene, garnet and magnesite that consumed the original hydrous melt and a very low proportion of a residual brine that precipitated chlorides (Förster et al. 2019).

Implications for the genesis of fibrous diamonds in the mantle wedge

It is remarkable that the inferred immiscible fluids trapped in garnet of the studied peridotite, a high-Mg carbonatite melt and a Na-K-Cl-F aqueous brine, correspond to the two types of high-density fluids found as inclusions in fibrous diamonds that crystallize in peridotites (Tomlinson et al. 2006; Klein-BenDavid et al. 2007; Weiss et al. 2009, 2015). In particular, Tomlinson et al. (2006) have reported fibrous coats in diamonds of the Panda kimberlites, that contain fluid inclusions consisting of coexisting brine and carbonatite melt, and were estimated to form at 930–1010 °C and 4.2–4.6 GPa. In addition, trace element analyses of the Panda diamond inclusions show an extreme enrichment in Ba, Th and LREE and a relative depletion in Nb, Ta, Ti and Zr (Tomlinson et al. 2009), similar to what is observed in the bulk rock trace element pattern of the garnet pyroxenite, source of the MSI. Hence MSI present in garnets of the studied peridotite might represent an example of lithospheric diamond-forming fluids, caught at a stage previous to the genesis of the diamond. These fluids may crystallize diamond at the appropriate P–T conditions when they enter a reducing mantle environment and interact with minerals of the host peridotite (e.g. Tomlinson et al. 2006). Such connection between sediment melts, their interaction with peridotites and the formation of fibrous diamonds with carbonate-brine inclusions has also been proposed by Förster et al. (2019).

Conclusions

The bulk compositions of primary multiphase solid inclusions in UHP rocks should not be directly equated to the composition of the originally trapped matrix fluid, as metasomatic and exchange reaction between trapped fluid(s) and host mineral can occur. To obtain information both on the nature of inclusions and related petrogenetic processes in the host rock, it is recommended to experimentally take the investigated inclusions to their P–T of entrapment.

In the studied case, the bulk compositions of primary multiphase solid inclusions present in garnets of UHP peridotites in the Bohemian Massif do not correspond to the compositions of a single matrix fluid trapped during growth of the coexisting garnet. Instead, they likely represent a mixture of trapped fluid(s) (a carbonatite melt ± coexisting brine), metasomatic minerals formed by reaction of fluid(s) and host garnet at trapped P–T (the Ba mica kinoshitalite ± olivine), that may have been further modified by metasomatic and exchange reaction of fluid(s) and host garnet upon cooling/exhumation (that produced amphibole).

We provide information on the partitioning of the lithophile element Ba during fluid-related processes at subarc depths (4.5 GPa, 1075 ºC): Ba is strongly compatible in carbonate melts and kinoshitalite with respect to a saline aqueous fluid, with a partitioning coefficient between carbonate melt and mica of c. 2.5–3. The extreme Ba enrichment in the inclusions in general, and carbonatite melt in particular, provides evidence that at least 80% of the major constituents (Si, Al, Ca and Na) of a parental subduction-related hydrous silicate-carbonate melt, were consumed during crystallization and melt-rock reaction in the mantle wedge, before generation of fluid(s) trapped in the studied inclusions.

Supplementary Information The online version contains supplementary material available at https://doi.org/10.1007/s00410-024-02132-1.

Acknowledgements This research was funded by the Czech Science Foundation (Projects 18-27454S and 22-33820S), the European Commission (Horizon 2020 Marie Skłodowska-Curie Actions), and the Ministry of Science and Innovation of Spain (Project PID2019-107718GB-100). The research has received funding from the European Union's Horizon 2020 research and innovation programme under the Marie Skłodowska-Curie grant agreement No. 654606. This publication is part of the project MALTA Consolider Team network (RED2022-134388-T), financed by MINECO/AEI/ https://doi.org/10.13039/501100003329. We thank C. Cantero and I.M. Sánchez-Almazo for assistence with EPMA and SEM analyses, respectively; and Prof. Müntener for the editorial work. We are grateful to four anonymous reviewers and Prof. Müntener for their thorough comments that greatly improved the clarity and consistency of the manuscript.

Funding Open Access funding provided thanks to the CRUE-CSIC agreement with Springer Nature.

Data availability The available data is provided in the article and supplementary material.

References

Alonso-Pérez R, Müntener O, Ulmer P (2009) Igneous garnet and amphibole fractionation in the roots of island arcs: experimental constraints on andesitic liquids. Contrib Mineral Petrol 157:541–558

Arai S, Ishimaru S (2008) Insights into petrological characteristics of the lithosphere of mantle wedge beneath arcs through peridotite xenoliths: a review. J Petrol 49:665–695

Arculus RJ (1994) Aspects of magma genesis in arcs. Lithos 33:189–208

Bartoli O, Cesare B, Poli S, Acosta-Vigil A, Esposito R, Turina A, Bodnar RJ, Angel RJ, Hunter J (2013) Nanogranite inclusions in migmatitic garnet: behavior during piston cylinder re-melting experiments. Geofluids 13:405–420

Cesare B, Acosta-Vigil A, Bartoli O, Ferrero S (2015) What can we learn from melt inclusions in migmatites and granulites? Lithos 239:186–216

Čopjaková R, Kotková J (2018) Composition of barian mica in multiphase solid inclusions from orogenic garnet peridotites as evidence of mantle metasomatism in a subduction zone setting. Contrib Mineral Petrol 173:1–18

Fiala J, Paděra K (1977) The chemistry of the minerals of the pyrope dunite from borehole T-7 near Staré (Bohemia). Tschermaks Mineral Petrogr Mitt 24:205–219

Foley SF (2011) A reappraisal of redox melting in the Earth's mantle as a function of tectonic setting and time. J Petrol 52:1363–1391

Foley SF, Yaxley GM, Rosenthal A, Buhre S, Kiseeva ES, Rapp RP, Jacob DE (2009) The composition of near-solidus melts of peridotite in the presence of CO_2 and H_2O between 40 and 60 kbar. Lithos 112S:274–283

Förster MW, Foley SF, Marschall HR, Alard O, Buhre S (2019) Melting of sediments in the deep mantle produces saline fluid inclusions in diamonds. Sci Adv 5:eaau2620

Frezzotti ML, Ferrando S (2015) The chemical behavior of fluids released during deep subduction based on fluid inclusions. Am Mineral 100:352–377

Gervasoni F, Klemme S, Rohrbach A, Grüzner T, Berndt J (2017) Experimental constraints on mantle metasomatism caused by silicate and carbonate melts. Lithos 282–283:173–186

Giuliani A, Pearson DG, Soltys A, Dalton H, Phillips D, Foley SF, Lim E, Goemann K, Griffin WL, Mitchell RH (2020) Kimberlite genesis from a common carbonate-rich primary melt modified by lithospheric mantle assimilation. Sci Adv 6:eaaz0424

Haifler J, Kotková J (2016) UHP-UHT peak conditions and near-adiabatic exhumation path of diamond-bearing garnet-clinopyroxene rocks from the Eger Cristalline Complex, North Bohemian Massif. Lithos 248–251:366–381

Haifler J, Kotková J, Čopjaková R (2024) Crystallization of trapped carbonate-silicate melts terminating at the carbonated solidus ledge – a record of carbon immobilization mechanism in the lithospheric mantle. Contrib Mineral Petrol 179:31

Hermann J, Rubatto D (2009) Accessory phase control on the trace element signature of sediment melts in subduction zones. Chem Geol 265:512–526

Hermann J, Spandler CJ (2008) Sediment melts at sub-arc depths: an experimental study. J Petrol 49:710–740

Hermann J, Zheng Y-F, Rubatto D (2013) Deep fluids in subducted continental crust. Elements 9:281–287

Kiseeva ES, Yaxley GM, Hermann J, Litasov KD, Rosenthal A, Kamenetsky VS (2012) An experimental study of carbonated eclogite at 3.5–5.5 GPa: Implications for silicate and carbonate metasomatism in the cratonic mantle. J Petrol 53:727–759. https://doi.org/10.1093/petrology/egr078

Klein-BenDavid O, Izraeli ES, Hauri E, Navon O (2007) Fluid inclusions in diamonds from the diavik mine, Canada and the evolution of diamond-forming fluids. Geochim Cosmochim Acta 71:723–744

Konzett J, Sweeney RJ, Thompson AB, Ulmer P (1997) Potassium amphibole stability in the upper mantle: an experimental study in a peralkaline KNCMASH system to 8.5 GPa. J Petrol 38:537–568

Kopecký L, Sattran V (1966) Buried occurrences of pyrope-peridotite and the structure of the crystalline basement in the extreme SW of the České středohoří Mts. Krystalinikum 4:65–86

Kotková J, O'Brien PJ, Ziemann MA (2011) Diamond and coesite discovered in Saxony-type granulite: solution to the Variscan garnet peridotite enigma. Geology 39:667–670

Kotková J, Čopjaková R, Skoda R (2021) Multiphase solid inclusions reveal the origin and fate of carbonate-silicate melts in metasomatised peridotite. Lithos 398–399:106309

Li W-Y, Yu H-M, Xu J, Halama R, Bell K, Nan X-Y, Huang F (2020) Barium isotopic composition of the mantle: Constraints from carbonatites. Geochim Cosmochim Acta 278:235–243

London D, Morgan VI GB, Acosta-Vigil A (2012) Experimental simulations of anatexis and assimilation involving metapelite and granitic melt. Lithos 153:292–307

Malaspina N, Hermann J, Scambelluri M, Compagnoni R (2006) Polyphase inclusions in garnet–orthopyroxenite (Dabie Shan, China) as monitors for metasomatism and fluid-related trace element transfer in subduction zone peridotite. Earth Planet Sci Lett 249:173–187

Mangan MT, Sisson TW, Hankins WB, Shimizu N, Vennemann T (2021) Constraints on deep, CO_2-rich degassing at arc volcanoes from solubility experiments on hydrous basaltic andesite of Pavlof Volcano, Alaska Peninsula, at 300 to 1200 MPa. Am Mineral 106:762–773

Manning CE (2004) The chemistry of subduction-zone fluids. Earth Planet Sci Lett 223:1–16

Martin LHJ, Schmidt MW, Mattsson HB, Guenther D (2013) Element partitioning between immiscible carbonatite and silicate melts for dry and H_2O-bearing systems at 1–3GPa. J Petrol 54:2301–2338

Massonne H-J (2001) First find of coesite in the ultrahigh-pressure metamorphic region of the Central Erzgebirge, Germany. Eur J Mineral 13:565–570

Massonne H-J, O´Brien PJ (2003) The Bohemian Massif and the NW Himalaya. In: Carswell DA, Compagnoni R (eds), Ultrahigh-pressure metamorphism. EMU notes in Mineralogy 5, Mineralogical Society of America, pp 145–187

McDonough WF, Sun S (1995) The composition of the Earth. Chem Geol 120:223–253

Medaris G, Wang H, Jelínek E, Mihaljevic M, Jakes P (2005) Characteristics and origins of diverse Variscan peridotites in the Gfohl Nappe, Bohemian Massif, Czech Republic. Lithos 82:1–23

Medaris LG, Ackerman L, Jelínek E, Michels ZD, Erban V, Kotková J (2015) Depletion, cryptic metasomatism, and modal metasomatism (refertilization) of Variscan lithospheric mantle: evidence from major elements, trace elements, and Sr-Nd-Os isotopes in a Saxothuringian garnet peridotite. Lithos 226:81–97

Philippot P (1993) Fluid-melt-rock interaction in mafic eclogites and coesite-bearing metasediments: constraints on volatile recycling during subduction. Chem Geol 108:93–112

Ravna EK (2000) Distribution of Fe^{2+} and Mg between coexisting garnet and hornblende in synthetic and natural systems: an empirical calibration of the garnet–hornblende Fe–Mg geothermometer. Lithos 53:265–277

Roedder E (1984) Fluid inclusions. Mineralogical Society of America, Reviews in Mineralogy 12, 644p

Schmädicke E, Evans BW (1997) Garnet-bearing ultramafic rocks from the Erzgebirge, and their relation to other settings in the Bohemian Massif. Contrib Mineral Petrol 127:57–74

Schmädicke E, Okrusch M, Schmidt W (1992) Eclogite facies rocks in the Saxonian Erzgebirge, Germany: high pressure metamorphism under contrasting P-T conditions. Contrib Mineral Petrol 110:226–241

Schmidt MW, Poli S (1998) Experimentally based water budgets for dehydrating slabs and consequences for arc magma generation. Earth Planet Sci Lett 163:361–379

Stepanov AS, Hermann J, Rubatto D, Korsakov AV, Danyushevsky LV (2016) Melting history of an ultrahigh-pressure paragneiss revealed by multiphase solid inclusions in garnet, Kokchetav Massif, Kazakhstan. J Petrol 57:1531–1554

Stöckhert B, Duyster J, Trepmann C, Massonne H-J (2001) Microdiamond daughter crystals precipitated from supercritical COH + silicate fluids included in garnet, Erzgebirge, Germany. Geology 29:391–394

Tatsumi Y, Eggins S (1995) Subduction zone magmatism. Wiley 224 pp

Tomlinson EL, Jones AP, Harris JW (2006) Co-existing fluid and silicate inclusions in mantle diamonds. Earth Planet Sci Lett 250:581–595

Tomlinson EL, Muller W, EIMF, (2009) A snapshot of mantle metasomtism: Trace element analysis of coexisting fluid (LA-ICP-MS) and silicate (SIMS) inclusions in fibrous diamonds. Earth Planet Sci Lett 279:362–372

Touret JLR (2001) Fluids in metamorphic rocks. Lithos 55:1–25

Weiss Y, Kessel R, Griffin WL, Kiflawi I, Klein-BenDavid O, Bell DR, Harris JW, Navon O (2009) A new model for the evolution of diamond-forming fluids: Evidence from microinclusions-bearing diamonds from Kankan, Guinea. Lithos 112:660–674

Weiss Y, McNeill J, Pearson DG, Nowell GM, Ottley CJ (2015) Highly saline fluids from a subducting slab as the source for fluid-rich diamonds. Nature 524:339–342

Whitney DL, Evans BW (2010) Abbreviations for names of rock-forming minerals. Am Mineral 95:185–187

Wirth R (2004) Focused ion beam (FIB); a novel technology for advanced application of micro- and nanoanalysis in geosciences and applied mineralogy. Eur J Mineral 16:863–876

Wirth R (2009) Focused ion beam (FIB) combined with SEM and TEM; advanced analytical tools for studies of chemical composition, microstructure and crystal structure in geomaterials on a nanometre scale. Chem Geol 261:217–229

Wyllie PJ (1988) Magma genesis, plate tectonics, and chemical differentiation of the Earth. Rev Geophys 26:370–404

Závada P, Stípská P, Hasalová P, Racek M, Jerábek P, Schulmann K, Kylander-Clark A, Holder R (2021) Monazite geochronology in melt-percolated UHP meta-granitoids: An example from the Erzgebirge continental subduction wedge, Bohemian Massif. Chem Geol 559:119919